SUBSPACE SWAP IMPROVEMENT TECHNIQUES FOR FINITE RATE OF INNOVATION SIGNAL RECONSTRUCTION

Thesis

Submitted in partial fulfillment of the requirements for the degree of
DOCTOR OF PHILOSOPHY

by

POKALA SUDHAKAR REDDY

DEPARTMENT OF ELECTRONICS AND COMMUNICATION ENGINEERING
NATIONAL INSTITUTE OF TECHNOLOGY KARNATAKA
SURATHKAL, MANGALORE-575025

DECEMBER, 2023

DECLARATION

I hereby ***declare*** that the research Thesis entitled **SUBSPACE SWAP IMPROVEMENT TECHNIQUES FOR FINITE RATE OF INNOVATION SIGNAL RECONSTRUCTION** which is being submitted to the ***National Institute of Technology Karnataka, Surathkal*** in partial fulfillment of the requirement for the award of the Degree of ***Doctor of Philosophy*** in **Department of Electronics and Communication Engineering** is a ***bonafide report of the research work carried out by me***. The material contained in this research Thesis has not been submitted to any University or Institution for the award of any degree.

P. Sudhakar Reddy

POKALA SUDHAKAR REDDY

Reg. No. 177075/177EC009

Department of Electronics and Communication Engineering.

Place: NITK Surathkal.

Date: 09-Dec-2023

CERTIFICATE

This is to certify that the Research Thesis entitled **SUBSPACE SWAP IMPROVEMENT TECHNIQUES FOR FINITE RATE OF INNOVATION SIGNAL RECONSTRUCTION** submitted by **POKALA SUDHAKAR REDDY** (Register Number: 177075/177EC009) as the record of the research work carried out by him, is accepted as the *Research Thesis submission* in partial fulfillment of the requirements for the award of degree of **Doctor of Philosophy**.

Dr. Raghavendra B.S.
Research Guide
Associate Professor
Dept. of Electronics and Communication Engg.
NITK Surathkal - 575025

Dr. A.V. Narasimhadhan
Research Guide
Associate Professor
Dept. of Electronics and Communication Engg.
NITK Surathkal - 575025

Prof. Neelawar Shekar Vittal Shet
Chairman-DRPC
Dept. of Electronics and Communication Engg.
NITK Surathkal - 575025

प्राध्यापक एवं विभागाध्यक्ष/PROF & HEAD
इ. एवं सी. विभाग / Department of E & C
एन.आई.टी.के. सुरत्कल/NITK Surathkal
मंगलूर / MANGALURU - 575 025

Acknowledgements

Firstly, I would like to express my sincere gratitude and deep regards to my research advisers Dr. Raghavendra B.S. and Dr. A. V. Narasimhadhan for their constant guidance and support provided throughout the course of this research work. Their patience, motivation and immense knowledge made me to accomplish this. I owe my deepest gratitude to their, also for bringing this thesis in the present form. I could not have imagined having a better advisers for my Ph.D.

Besides my advisers, I express my gratitude to Prof. Neelawar Shekar Vittal Shet, Head of the department, ECE for the constant support and encouragement. My sincere thanks goes to Prof. U. Shripathi Acharya, Head, Dept. of ECE during my enrollment for Ph.D. program for his help and invaluable suggestions. Also, I thank Prof. Laxminidhi T., Prof Ashvini Chaturvedi, Heads, Dept. of ECE during my research work for his support and help. My sincere thanks to Dr. Alwyn Roshan Pais, Dr. Shyam Lal, RPAC members, for their invaluable suggestions during every step of my progress in the research work.

I would like to thank all the faculty and staff of ECE department, NITK Surathkal. I also thank the staff in Academic, Admission and Cash sections of NITK for their assistance.

I would like to express my gratitude to all friends and colleagues at NITK for encouraging me in good and bad times making a memorable stay in NITK. Special thanks to my labmates, Palla Parasuram and Sravan Kumar Padala for their constant help in solving MATLAB tool related issues. I also thank M.Tech. students A. Premkumar and B. Saikiran who helped me in understanding deep learning.

I would like to thank my parents Narayana Reddy and Subbamma, wife Rajeswari, brother Ayyavaru Reddy for their continuous support, love, and encouragement.

I am deeply indebted to all my teachers throughout life, who have guided, encouraged, and inspired me to grow in both technical and personal aspects.

Finally, I would like to thank god for giving me good health, strength, and bliss during my research work.

My Dear Parents & Brother

Abstract

Finite rate of innovation (FRI) framework has been developed for sampling and reconstruction of a class of continuous non-bandlimited signals known as signals with FRI. This is achieved utilizing suitable sampling kernels and reconstruction techniques. The FRI framework has been extended to discrete-time sparse signals for reconstruction. However, some reconstruction algorithms tend to breakdown at certain signal-to-noise ratios (SNR) due to subspace swap. In this thesis, we propose novel strategies to improve reconstruction performance in the breakdown region.

First, we propose a universal FRI scheme based on the error decrease detector criterion which enables reconstructing sparse signals with an unknown number of nonzero coefficients. The scheme accomplishes perfect reconstruction in the noiseless scenario. An extension of the scheme is presented for the noisy case. When compared to the conventional scheme, the proposed scheme exhibits improvements in performance in the breakdown SNR. In addition, an application of the proposed FRI scheme for reconstructing magnetic resonance imaging (MRI) and electrocardiogram (ECG) is demonstrated.

Next, we propose a sparse-Prony method which avoids polynomial root-finding for reconstructing streams of Diracs. The method produces perfect reconstruction in a noise-free environment. Extensive simulations are carried out to compare the performance of sparse-Prony with that of Prony's and matrix pencil methods for noisy cases, and the results demonstrate superior performance of the sparse-Prony method. We also provide a residual neural network approach which iteratively works on the training data for reconstructing streams of Diracs. The simulation results on synthetic noisy data have shown better reconstruction performance in the breakdown region when compared with the Prony's and matrix pencil methods.

Finally, we introduce a novel technique to estimate seismic reflectivity signals using the FRI theory which helps determine the subsurface structure. The seismic data is modelled as a convolution between the Ricker wavelet and the FRI signal-a Dirac impulse train. The experimental results have demonstrated comparable reflectivity estimation performance with lesser

data in the noiseless and medium to high SNR regimes.

Keywords: Finite rate of innovation; sampling; reconstruction; subspace swap; sparse signal; Prony's method; seismic reflectivity.

Contents

List of Figures

List of Tables

Abbreviations

AMP	Approximate message passing
DFT	Discrete Fourier transform
ECG	Electrocardiogram
EEG	Electroencephalogram
ERK	Exponential reproducing kernel
FRI	Finite rate of innovation
FT	Fourier transform
GS	Gibbs sampler
GSFC	Generalized Strang-Fix conditions
LARS	Least angle regression
LT	Laplace transform
MAE	Mean absolute error
MR	Magnetic resonance
MRI	Magnetic resonance imaging
MSE	Mean squared error
NL	Noiseless
OMP	Orthogonal matching pursuit
PRK	Polynomial reproducing kernel
ResNet	Residual neural network
SFC	Strang-Fix conditions
SNR	Signal-to-noise ratio
SVD	Singular value decomposition
TLS	Total least square
TV	Total variation

Notations and formulas

$\mathbb{Z}$	Integers
$\mathbb{R}$	Real numbers
$\mathbb{C}$	Complex numbers
$[c, d]$	Closed interval: $\{x \in \mathbb{R} : c \leq x \leq d\}$
(c, d)	Open interval: $\{x \in \mathbb{R} : c < x < d\}$
$[c, d)$	Left-closed, right-open interval: $\{x \in \mathbb{R} : c \leq x < d\}$
$(c, d]$	Left-open, right-closed interval: $\{x \in \mathbb{R} : c < x \leq d\}$
$g(t)$	Continuous-time signal
$g[n]$	Discrete-time signal
$\langle g(t), f(t) \rangle$	Inner product: $\int_{-\infty}^{\infty} g(t) f^*(t) dt$
$\langle g[n], f[n] \rangle$	Inner product: $\sum_{n=-\infty}^{\infty} g[n] f^*[n]$
$\delta(t)$	Dirac distribution: $\int_{-\infty}^{\infty} \delta(t) g(t) dt = g(0)$
$\delta[n]$	Discrete Dirac: 1 if $n = 0$, 0 otherwise
$g(t) * t(t)$	Continuous-time convolution: $\int_{-\infty}^{\infty} g(u) f(t-u) du$
$g[n] * f[n]$	Discrete-time convolution: $\sum_{k=-\infty}^{\infty} g[k] f[n-k]$
$g \in \mathbb{R}^N$	Finite-dimensional vector of size $N : g = (g[n])_{n=0}^{N-1}$
$P \in \mathbb{C}^{L \times N}$	Matrix of size $L \times N$
P^T	Transpose of Matrix P
P^H	Hermitian transpose of Matrix P
$FT\{g(t)\} = \hat{g}(w)$	Fourier transform: $\int_{-\infty}^{\infty} g(t) e^{-jwt} dt$
$LT\{g(t)\} = \hat{g}(s)$	Laplace transform: $\int_{-\infty}^{\infty} g(t) e^{-st} dt$
$DFT\{g[n]\} = \hat{g}[l]$	Discrete Fourier transform: $\left(\frac{1}{\sqrt{N}} \sum_{n=0}^{N-1} g[n] e^{-j2\pi nl/N} \right)_{l=0}^{N-1}$

Chapter 1

INTRODUCTION

1.1 Motivation

Real-life signals are typically analog and to be processed by digital systems, we must first discretize them, which is known as sampling. In the typical sampling configuration, the original analog signal $g(t)$ is filtered using a sampling kernel $\varphi(t)$, with impulse response $h(t) = \varphi(-t/T)$ and then sampled according to sampling interval T leads to the discrete signal $f[n] = g(t) * h(t)|_{t=nT}$. The filtering may be caused by the acquisition device or by a design choice. Signal acquisition model is depicted in the Fig. 1.1. One apparent question that emerges at this stage is whether it is possible to reconstruct $g(t)$ using only information from the samples $f[n]$.

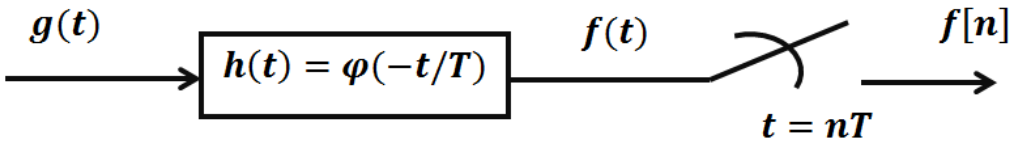

Figure 1.1: Signal acquisition model, $g(t)$ is analog signal, $h(t)$ is impulse response of the acquisition device which is scaled and time reversed version of the sampling kernel $\varphi(t)$, and T is the sampling period.

Since sampling involves an inherent loss of information, we will never be able to recover the signal $g(t)$ from the sampled sequence $f[n]$. However, there are certain conditions where the signal $g(t)$ can be recovered, depending on the characteristics of $h(t)$, the signal's type $g(t)$, and the sampling interval T. The most famous and

commonly used sampling theorem, attributed to Shannon established a necessary condition for perfect recovery of bandlimited signals using the sinc function. The signal can be exactly recovered from its sampled sequence if the sampling frequency $1/T$ is greater than or equal to twice the maximum frequency of the signal.

In the past years, a novel sampling framework has been presented for specific classes of non-bandlimited signals. Specifically, these signals are parametric and are described by a finite number of free parameters per unit time interval. The number of free parameters per unit time interval is referred to as the rate of innovation. Therefore, the new framework is known as the finite rate of innovation (FRI) theory. FRI theory permits sampling and exact reconstruction of FRI signals at a rate defined by the number of free parameters per unit time interval rather than the signal's maximum frequency, utilizing suitable sampling functions and reconstruction methods.

The concept of reconstructing a signal from partial information can also be applied to discrete signals. In this instance, the input signal is a N-dimensional vector g, and assume we have access to an L-dimensional vector named f, with $L < N$. Further, we assume that the two vectors are linearly related, using the equation $f = Pg$, where P is a matrix of dimension $L \times N$. Generally, $L < N$ makes this an unsolvable underdetermined system of equations. Therefore, we need to impose some restrictions on the vector g. In this context, sparse vectors-vectors with a minimal number of non-zero elements are taken into consideration, which is having finite number of free parameters similar to the signal in continuous-time FRI framework. There are methods where g can be exactly reconstructed from the measured vector f, based on the precise structure of the matrix P. FRI hypothesis has a variety of applications, including electroencephalogram (EEG), electrocardiogram (ECG), magnetic resonance imaging (MRI), functional MRI, and calcium imaging.

1.2 Literature survey

In the literature, it has been demonstrated that some non-bandlimited signals can be sampled and perfectly reconstructed (Vetterli *et al.* 2002, Dragotti *et al.* 2007). Such signals are referred to as FRI signals as they possess the feature of having a parametric representation with a finite number of free parameters. A Dirac impulse train, differential Diracs, piecewise polynomials, and nonuniform splines are few examples of FRI signals. An annihilating filter method (Prony's method) (Vetterli *et al.* 2002,

Dragotti *et al.* 2007), a tool frequently used in spectral estimation, has been used for reconstructing the FRI signals.

Prony's method needs to solve annihilation equation which leads to an unstable reconstruction when measurement samples are corrupted by noise, and many FRI reconstruction algorithms exist to improve resiliency to noise. There are techniques based on denoising the measurements before applying the Prony's method. This operation is carried out utilizing structured low rank approximation (Markovsky 2008) and utilizing Cadzow denoising (Cadzow 1988, Blu *et al.* 2008). The other techniques employ subspace decomposition such as matrix pencil method (Hua and Sarkar 1990), to reconstruct the free parameters directly. This strategy is initially introduced for FRI (Maravic and Vetterli 2005) and is later make use of (Erdozain and Crespo 2011, Urigüen *et al.* 2013). In addition, there are stochastic algorithms for FRI reconstruction such as Gibbs sampler (GS) (Tan and Goyal 2008), GS with a genetic algorithm in (Erdozain and Crespo 2010), iterative maximum likelihood (Wein and Srinivasan 2013) and modified local best particle swarm optimization (Najjarzadeh and Sadjedi 2020). Recently, deep neural networks (Leung *et al.* 2020, 2021) have been used, which involves learning from training data (measurements) and gives signal parameters directly. The sparsity-based method (Huang *et al.* 2016) make use of sparsely represented measurements, and then parameters are estimated by resolving an optimization problem in terms of L0 norm.

A large number of sampling kernels are employed for reconstructing FRI signals. Infinite support kernels, such as sinc (ideal low-pass filter) (Vetterli *et al.* 2002, Maravic and Vetterli 2005, Blu *et al.* 2008) and Gaussian kernels (Vetterli *et al.* 2002, Maravic and Vetterli 2005, Erdozain and Crespo 2011, Tan and Goyal 2008, Erdozain and Crespo 2010), are physically unrealizable, whereas polynomial-reproducing (Dragotti *et al.* 2007), and exponential reproducing kernels (Urigüen *et al.* 2013, Leung *et al.* 2020, Huang *et al.* 2016) have finite support. While they permit perfect reconstruction in environments free of noise, their behavior alters when noise is present. When the parameters are purely imaginary, the exponential reproducing kernel allows for more stable reconstruction. In order to increase the resiliency to noise of unstable kernels such as polynomial-reproducing, Gaussian or sinc kernels, (Urigüen *et al.* 2013) proposed a new FRI framework. This extends the traditional framework to any kernel (universal FRI), which needs an implied design to satisfy the exponential reproduction limitation of generalised approximate Strang-Fix condition.

The FRI framework has been extended to reconstruct discrete-time signals by (Hormati and Vetterli 2007). In this case, the input signal is a high-dimensional vector that has just a few nonzero values and many zero values (sparse signal). The observed signal is a low-dimensional vector that is obtained by multiplying the input signal with a partial unitary discrete Fourier transform matrix (DFT). The parameters of the input signal (i.e. nonzero positions and their intensity values) are estimated by applying the Prony's method. More recently, (Oñativia *et al.* 2014) developed a finite-dimensional FRI technique which gives better performance than the matrix pencil method and Prony's method.

1.3 Sampling signals with FRI

(Vetterli *et al.* 2002) have introduced a FRI framework for sampling and reconstruction of a class of parametric non-bandlimited signals. Such signals are specified by a small number of information (free) parameters per unit of time and are called FRI signals.

In this section, we begin by providing a mathematical formulation for FRI signals and examples of signals with FRI. Next, the various components of the sampling configuration for sampling FRI signals are shown and thoroughly explored, including sampling functions and reconstruction techniques. Finally, we present the applications of FRI theory.

1.3.1 Definition of signals with FRI

Consider signals of the form

$$g(t) = \sum_{r\in\mathbb{Z}} \sum_{k=0}^{K} a_{k,r} \nu_k(t - t_r) \tag{1.1}$$

where $\{\nu_k(t)\}_{k=0}^{K}$ is a collection of well-known functions. The parameters $a_{k,r}$ and t_r are degrees of freedom also known as information parameters. Let $\zeta_g\left(-\frac{\tau}{2}, +\frac{\tau}{2}\right)$ be a function which computes number of information parameters in $g(t)$ over the range $\left(-\frac{\tau}{2}, +\frac{\tau}{2}\right)$. For the equation of $g(t)$ in (1.1), we have that

$$\zeta_g\left(-\frac{\tau}{2}, +\frac{\tau}{2}\right) = (K+2)\left|\{t_r \in \left(-\frac{\tau}{2}, +\frac{\tau}{2}\right)\}\right| \tag{1.2}$$

where $|\{t_r \in \left(-\frac{\tau}{2}, +\frac{\tau}{2}\right)\}|$ represents the number of t_r in $\left(-\frac{\tau}{2}, +\frac{\tau}{2}\right)$. The rate of innovation ρ is expressed as

$$\rho = \lim_{\tau \to \infty} \frac{1}{\tau} \zeta_g \left(-\frac{\tau}{2}, +\frac{\tau}{2}\right) \tag{1.3}$$

A signal with FRI is a signal whose parametric form is provided in (1.1) and has a finite ρ as stated in (1.3) (Vetterli *et al.* 2002, Dragotti *et al.* 2007).

1.3.2 Examples of signals with FRI

During the development of the FRI framework, the stream of Diracs, stream of differential Diracs, and piecewise polynomials have been explored (Vetterli *et al.* 2002, Dragotti *et al.* 2007). These examples are specified over the interval [0,1) for simplicity and are simple to extend to other intervals. Using equation (1.1), a stream of R Dirac impulses can be expressed as

$$g(t) = \sum_{r=0}^{R-1} a_r \delta(t - t_r). \tag{1.4}$$

Since the r-th impulse is characterized by its amplitude a_r and its delay $t_r \in [0, 1)$, the rate of innovation for the signal $g(t)$ is given as $2R$. The stream of Dirac impulses (1.4) can be easily extended as a train of pulses by directly substituting the Dirac shape $\delta(t)$ with the well-known pulse shape. Similarly, a train of R differentiated Diracs with time delays $\{t_r\}_{r=0}^{R-1}$ and amplitudes $\{a_{r,j}\}_{r=0,j=0}^{R-1,J_r-1}$ can be expressed as suitably displaced and weighted linear combinations of differentiated Diracs, i.e,

$$g(t) = \sum_{r=0}^{R-1} \sum_{j=0}^{J_r-1} a_{r,j} \delta^{(j)}(t - t_r) \tag{1.5}$$

where $\delta^{(j)}$ is the j-th derivative of Dirac which is described as a distribution that meets the criteria below

$$\int_{-\infty}^{\infty} u(t) \delta^{(j)}(t - t_0) dt = (-1)^j u^{(j)}(t_0). \tag{1.6}$$

A signal of this type has R delays and $\sum_{r=0}^{R-1} J_r$ different weights. Thus, it has a rate of innovation of $R + \sum_{r=0}^{R-1} J_r$. Finally, piecewise polynomials with R segments of maximal

degree $J-1$ have the following equation

$$g(t) = \sum_{r=0}^{R-1} \sum_{j=0}^{J-1} a_{r,j} (t - t_r)_+^j \tag{1.7}$$

The rate of innovation of this type of signal is given by $R + RJ$ because the J-th derivative of this signal generates a train of R differential Diracs, i.e

$$g^{(J)}(t) = \sum_{r=0}^{R-1} \sum_{j=0}^{J-1} a_{r,j} \delta^{(j)}(t - t_r) \tag{1.8}$$

1.3.3 Sampling kernels

In a typical FRI acquisition process, first, the input signal is convolved with a sampling kernel and then sampled at uniform time locations. The sampling kernel is crucial for both signal acquisition and reconstruction. There are employed a large number of sampling kernels for reconstructing non-bandlimited signals as dealt with in the FRI sampling schemes. (Vetterli *et al.* 2002), sinc and Gaussian kernels are proposed which have an infinite duration and are therefore physically non-realizable

$$Sinc \qquad \varphi(t) = sinc(t) = \frac{sin(\pi t)}{\pi t} \tag{1.9}$$

$$Gaussian \qquad \varphi(t) = e^{-t^2/2\alpha^2}. \tag{1.10}$$

To overcome this problem, (Dragotti *et al.* 2007) proposed a class of finite support kernels which includes exponential and polynomial reproducing functions.

Polynomial reproducing kernels

Any function that shifting, weighting, and summing can generate polynomial functions termed as polynomial reproducing kernel (PRK), i.e,

$$\sum_{n \in \mathbb{Z}} c_{l,n} \varphi(t - n) = t^l, \tag{1.11}$$

where $l = 0, 1, 2....P$, P is the order of PRK, and $c_{l,n} \in \mathbb{C}$. PRKs for which (1.11) is correct fulfill the so-called Strang-Fix conditions (SFC):

$$\widehat{\varphi}(0) \neq 0 \quad and \quad \widehat{\varphi}^{(l)}(2\pi q) = 0 \quad for \quad q \in \mathbb{Z} - \{0\} \quad and \quad l = 0, 1, 2.....P. \tag{1.12}$$

where $\widehat{\varphi}(2\pi q)$ is Fourier transform (FT) of $\varphi(t)$ at $w = 2\pi q$ and superscript (l) represents the l-th derivative.

The basis splines, or B-splines, a word Schoenberg created, are a flexible family of functions that meet these requirements. Splines are typically piecewise polynomials with a maximum degree P. The term "knots" refers to the extreme points of the intervals that constitute the pieces. The splines exhibit significant smoothness at these knots since they are differentiable up to order $P - 1$. Consider the following function

$$\kappa_0(t) = 1, 0 \leq t < 1 \quad \xrightarrow{\text{FT}} \quad \widehat{\kappa}_0(\omega) = \frac{1 - e^{-j\omega}}{j\omega}, \tag{1.13}$$

which characterizes a B-spline of zero order and meets the SFC specified in (1.12) with $P = 0$. As a result, zero-order polynomials can be reproduced by $\kappa_0(t)$. Recursively convolving lower-order B-splines results in the construction of higher-order ones, i.e,

$$\kappa_P(t) = \kappa_{P-1}(t) * \kappa_0(t) \quad \xrightarrow{\text{FT}} \quad \widehat{\kappa}_P(\omega) = \left(\frac{1 - e^{-j\omega}}{j\omega}\right)^{P+1}. \tag{1.14}$$

The above function also fulfills the SFC therefore, polynomials of order up to P can be reproduced by $\kappa_P(t)$. We must calculate the $c_{l,n}$ coefficients to generate a particular polynomial t^l. The coefficients $c_{l,n}$ can be determined from quasi-biorthonormal set $\{\psi(t-n)\}_{n\in\mathbb{Z}}$ as $c_{l,n} = \langle t^l, \psi(t-n)\rangle$ where $\psi(t)$ is dual of $\varphi(t)$, i.e. $\langle \varphi(t), \psi(t-n)\rangle = \delta[n]$. In this instance, we have

$$c_{l,n} = \int_{-\infty}^{\infty} t^l \psi(t-n) dt \tag{1.15}$$

$$= \int_{-\infty}^{\infty} (t+n)^l \psi(t) dt \tag{1.16}$$

$$= \sum_{k=0}^{l} l_{c_k} n^{l-k} \int_{-\infty}^{\infty} t^k \psi(t) dt \tag{1.17}$$

$$= \sum_{k=0}^{l} l_{c_k} n^{l-k} c_{k,0}. \tag{1.18}$$

Substituting the above equation for $c_{l,n}$ in (1.11) we obtain

$$c_{l,0} = \frac{t^l - \sum_{k=0}^{l-1} l_{c_k} c_{k,0} \sum_{n\in\mathbb{Z}} n^{l-k} \varphi(t-n)}{\sum_{n\in\mathbb{Z}} \varphi(t-n)} \qquad l = 0, 1, 2.....P. \tag{1.19}$$

Exponential reproducing kernels

Any function that shifting, weighting, and summing can generate exponential functions termed as exponential reproducing kernel (ERK), i.e,

$$\sum_{n\in\mathbb{Z}} c_{l,n} \varphi(t-n) = e^{\alpha_l t}, \tag{1.20}$$

where $l = 0, 1, 2....P$, P is the order of ERK, $\alpha_l \in \mathbb{C}$ and $c_{l,n} \in \mathbb{C}$. ERKs for which (1.20) is correct fulfill the so-called generalized SFC (GSFC):

$$\widehat{\varphi}(\alpha_l) \neq 0 \quad and \quad \widehat{\varphi}(\alpha_l + j2\pi q) = 0 \quad for \quad q \in \mathbb{Z} - \{0\} \quad and \quad l = 0, 1, ..., P, \tag{1.21}$$

where $\widehat{\varphi}(\alpha_l)$ is Laplace transform (LT) of $\varphi(t)$ at $s = \alpha_l$.

A class of spline theory functions known as exponential splines (E-splines) are particularly suitable for exponential reproduction. The theory concerning E-splines, which can reproduce exponential functions, is presented by M. Unser in 2005. Consider the following function

$$\kappa_\alpha(t) = e^{\alpha t}, 0 \leq t < 1 \quad \xrightarrow{\text{LT}} \quad \widehat{\kappa}_\alpha(s) = \frac{1 - e^{\alpha - s}}{s - \alpha}. \tag{1.22}$$

which characterizes a E-spline of zero order with parameter α that can reproduce exponential function $e^{\alpha t}$. Higher-order E-splines are obtained through successive convolutions of zero order ones, i.e,

$$\kappa_{\overrightarrow{\alpha}}(t) = \kappa_{\alpha_0}(t) * \kappa_{\alpha_1}(t) * ..... * \kappa_{\alpha_P}(t) \quad where \quad \overrightarrow{\alpha} = (\alpha_0, \alpha_1, ..., \alpha_P). \tag{1.23}$$

The above function fulfills the GSFC therefore, a set of $P+1$ exponentials of the type $\{e^{\alpha_l t}\}_{l=0}^{P}$ can be reproduced by $\kappa_{\overrightarrow{\alpha}}(t)$. Similar to the polynomial case, to reproduce a

particular exponential $e^{\alpha_l t}$, the coefficients $c_{l,n}$ in (1.20) are provided by

$$c_{l,n} = \langle e^{\alpha_l t}, \psi(t-n) \rangle, \tag{1.24}$$

where $\psi(t)$ is dual of $\varphi(t)$. In this instance, we have

$$c_{l,n} = \int_{-\infty}^{\infty} e^{\alpha_l t} \psi(t-n) dt \tag{1.25}$$

$$= \int_{-\infty}^{\infty} e^{\alpha_l (t+n)} \psi(t) dt \tag{1.26}$$

$$= e^{\alpha_l n} \int_{-\infty}^{\infty} e^{\alpha_l t} \psi(t) dt \tag{1.27}$$

$$= e^{\alpha_l n} c_{l,0} \tag{1.28}$$

Substituting the above equation for $c_{l,n}$ in (1.20) we obtain

$$c_{l,0} = [\widehat{\varphi}(\alpha_l)]^{-1} \quad and \quad c_{l,n} = e^{\alpha_l n} [\widehat{\varphi}(\alpha_l)]^{-1}. \tag{1.29}$$

When parameters $\alpha_l = jw_l$ are purely imaginary, the ERK finds its application in stable reconstruction even in the presence of noise.

1.3.4 Reconstruction methods

The parameters that represent FRI signal (stream of R Dirac impulses) sampled by suitable sampling functions can be obtained by converting the set of measurement samples into a power sum form (Kusuma and Goyal 2008) that is identical to the

$$q[l] = \sum_{r=1}^{R} b_r \mu_r^l \tag{1.30}$$

for $l = 0, 1, ..., P$. In this case, we are interested in obtaining parameters b_r and μ_r from the power sum sequence (1.30). The spectrum estimation community has spent years studying the problem of determining the parameters of the power sum sequence given a set of samples, which occurs in different fields such as thermal imaging, array processing, geophysical inversion, and computed tomography (Elad *et al.* 2004). Here, finding the nonlinear parameters μ_r is the biggest challenge. There are many

reconstruction techniques proposed, (Vetterli *et al.* 2002) proposed the annihilating filter method (Prony's method).

Prony's method

Prony's method main principle is as follows: consider filter $\mathbf{d}$ with R zeros at μ_r in Z-transform $D(z) = \prod_{r=1}^{R}(1 - \mu_r z^{-1})$. It follows that

$$q[l] \star \mathbf{d}[l] = \sum_{u=0}^{R} \mathbf{d}[u]q[l-u] = 0. \tag{1.31}$$

The filter $\mathbf{d}$ is known as an annihilating filter because it annihilates the sequence of samples $q[l]$. The above identity is written in matrix notation as follows

$$Q\mathbf{d} = 0, \tag{1.32}$$

where Q is the Toeplitz matrix of size $(P-R+1)\times(R+1)$ and $\mathbf{d}$ is the annihilating filter of size $(R+1)\times(1)$. If $P+1 \geq 2R$, the filter $\mathbf{d}$ is estimated from (1.32) as null-space of Q and then retrieved μ_r by calculating the polynomial roots of D. Finally, parameters b_r are determined by solving the system of equations in (1.30).

In the noisy scenario, Prony's method has been modified by using the total least square (TLS) solution, which results in an approximate solution. The major disadvantage of Prony's method is that the reconstruction performance worsens when signal samples are corrupted with noise. To improve the reconstruction performance, Cadzow iterative algorithm is presented before applying Prony's method (Blu *et al.* 2008). Alternatively, (Maravic and Vetterli 2005, Urigüen *et al.* 2013) presented the direct matrix pencil method, which has shown a similar performance as that of annihilating filter method with the Cadzow algorithm. The matrix pencil algorithm consists of the following steps.

Matrix pencil method

First, we build Toeplitz matrix Q from power sum sequence $q[l]$ in (1.30). Next, the matrix Q_s is obtained by keeping the left-singular vectors corresponding to the R biggest singular values in singular value decomposition (SVD) of Toeplitz matrix Q. Let Q_1, Q_2 be the matrices created from matrix Q_s by eliminating the first and last

rows, respectively. Then, the parameters μ_r are retrieved by eigenvalues of $Q_2^+ Q_1$, where Q_2^+ represents pseudoinverse Q_2. Finally, from μ_r and samples $q[l]$, parameters b_r are determined by solving the system of equations in (1.30).

The above FRI reconstruction algorithms use SVD for estimating the signal subspace which gives optimal results up to a certain signal-to-noise ratio (SNR) and worsen (this is referred to as breakdown) when the SNR falls below a certain threshold. Reason for the same is the occurrence of subspace swap wherein there may occur interchange of signal and orthogonal subspaces under noisy conditions (Wei and Dragotti 2015). The condition for subspace swap depends on the parameters such as standard deviation corresponding to SNR, least singular value of signal, and number of measurements.

1.3.5 Applications

The notion of the FRI framework has been investigated in several signal processing applications. The outcomes are encouraging in applications like:

- Compression of ECG and EEG signals (Baechler *et al.* 2013, Poh and Marziliano 2010).
- Reduction of scan time in MRI (Deslauriers-Gauthier and Marziliano 2011*a*, Sudhakar Reddy *et al.* 2020).
- Estimation of spikes in two-photon calcium imaging (Onativia *et al.* 2013*a*).
- Estimation of spontaneous brain activity in functional MRI (Doğan *et al.* 2014).
- Image super-resolution methods (Baboulaz and Dragotti 2009).
- Ultrasound image reconstruction (Mulleti *et al.* 2014).

1.4 Thesis contribution

Even though the FRI theory has advanced significantly over the past few years, its potential has not yet been completely realized. The reason is that the reconstruction of FRI signals is a non-linear task and some algorithms reported in the literature can produce poor results during break-down and are unstable due to subspace swap.

Therefore, the goal is to enhance the performance of algorithms during break-down. Moreover, investigating potential FRI theory expansions for other applications is also important.

Based on the above requirements, we framed the three objectives in the context of continuous and discrete-time scenarios. In particular, in the discrete-time case, universal FRI scheme is introduced based on the error reduction detector criterion that allows for the reconstruction of sparse signals with an unknowable number of nonzero coefficients. The scheme achieves perfect reconstruction in the event of noiseless settings. For the noisy scenario, the extension of the scheme is provided. The proposed scheme shows improvements in the breakdown SNR when compared to the traditional scheme. Additionally, a demonstration of the proposed FRI scheme's use with MRI and ECG data is shown.

Whereas, in the continuous-time case, we presented a polynomial root-free sparse-Prony approach for reconstructing streams of Diracs. The technique produces perfect reconstruction in a noise-free setting. We run in-depth simulations to compare sparse-Prony method performance in a noisy environment to that of Prony's and matrix pencil approaches, which are more widely used. For reconstructing streams of Diracs, additionally offer a residual neural network and they perform better in breakdown SNR than traditional ones. Further, an application of the proposed sparse-Prony approach is demonstrated to retrieve the timing of action potentials from calcium transient time series.

Additionally, in the continuous-time case, we presented a novel method for estimating the seismic data's reflectivity signal using the FRI theory, which aids in understanding the subsurface structure. The convolution of the FRI signal, a Dirac impulse train, and the Ricker wavelet are used to represent the seismic data. The experimental results show that the suggested method requires lesser data while still producing comparable reflectivity estimation performance for noiseless and medium to high SNR regimes.

1.5 Thesis organization

The rest of the thesis is organized as follows.

- In Chapter 2, the universal discrete FRI scheme for sparse signal reconstruction is presented. Further, an application of the proposed scheme on reconstruction

of MRI and ECG is demonstrated.

- In Chapter 3, the sparse-Prony and residual neural network approaches for FRI signal reconstruction are presented. Further, an application of the proposed sparse-Prony on two-photon calcium imaging is demonstrated.
- In Chapter 4, the approximate FRI-based seismic reflectivity estimation is presented.
- Conclusion and future work are presented in Chapter 5.

Chapter 2

UNIVERSAL DISCRETE FRI SCHEME FOR SPARSE SIGNAL RECONSTRUCTION

2.1 Introduction

In the discrete finite rate of innovation (FRI) schemes, reconstruction methods such as "Cadzow + Prony" (Blu *et al.* 2008), matrix pencil (Urigüen *et al.* 2013), and "Cadzow + finite-dimensional FRI" (Oñativia *et al.* 2014) involve using singular value decomposition (SVD). The trick here is partitioning the measurement space into a signal subspace and a noise subspace. These methods achieve optimal results up to a certain signal-to-noise ratio (SNR). When SNR drops below a threshold, reconstruction becomes highly unstable due to subspace swap (Wei and Dragotti 2015). Moreover, these reconstruction schemes are not universal, as they necessitate the knowledge of the number of nonzero coefficients (L0 norm) for proper reconstruction.

Recently, several universal schemes have been proposed for sampling and reconstruction of FRI signals based on minimum error (Wei and Dragotti 2014, Gilliam and Blu 2014), mean squared error (Gilliam and Blu 2016) and error decrease detector criteria (Wei and Dragotti 2017). In this chapter, we reformulate a scheme based on the error decrease detector criterion in the context of a discrete-time case which is more efficient and has less computational complexity than other cases. Simulations are carried out for noiseless and noisy cases to verify performance of the universal FRI scheme. Further, the proposed universal framework is extended to reconstruct

magnetic resonance (MR) images and QRS complexes from sparse data.

The chapter is organized as follows: Section 2.2 describes universal FRI scheme considering noiseless and noisy scenarios to recover signals with an unknown number of nonzero coefficients. Section 2.3 presents simulations of the proposed FRI scheme. Section 2.4 describes method to reconstruct MR images and QRS complexes based on the proposed scheme and presents simulation results. Finally, the chapter is summarized in Section 2.5.

2.2 Universal discrete FRI scheme

In this section, we introduce universal FRI scheme to reconstruct sparse signals with an unknown number of nonzero coefficients. Separate discussions are given to reconstruction schemes with and without noise instances.

2.2.1 Reconstruction of sparse signal in absence of noise

Assume that the input $g \in \mathbb{R}^N$ is a sparse signal with R nonzero coefficients

$$g[n] = \sum_{r=1}^{R} a_r \delta[n - n_r], \qquad n = 0, 1, 2, ..., N-1. \tag{2.1}$$

The signal $g[n]$, also known as discrete FRI signal with a rate of innovation $\frac{2R}{N}$ as it is fully characterized by integer positions $n_r \in [0, N-1]$ and real intensities a_r. Consider the acquisition of $L < N$ observations of g as

$$f = Pg, \tag{2.2}$$

where $g = [g[0]g[1]...g[N-1]]^T$, $f = [f[0]f[1]...f[L-1]]^T \in \mathbb{C}^L$ is the observed signal, and $P \in \mathbb{C}^{L \times N}$ is the acquisition (fat) matrix. For acquisition, we employ partial unitary discrete Fourier transform (DFT) matrix $(P)_{l \times n} = e^{-j2\pi ln/N}/\sqrt{N}$ with $l = 0, 1, 2, ..., L-1$ and $n = 0, 1, 2, ..., N-1$ as proposed by (Oñativia *et al.* 2014). The entries in the observed signal f are the DFT coefficients of g given by

$$f[l] = \frac{1}{\sqrt{N}} \sum_{r=1}^{R} a_r e^{-j2\pi n_r l/N} = \frac{1}{\sqrt{N}} \sum_{r=1}^{R} a_r \eta_r^l, \qquad l = 0, 1, 2, ..., L-1, \tag{2.3}$$

where $\eta_r = e^{-j2\pi n_r/N}$. Given the observations, the next step is to reconstruct original input signal $g[n]$. To achieve this, a novel reconstruction scheme is presented based on the error decrease detector criterion (stopping criterion) which extends the scheme in (Oñativia *et al.* 2014) to a universal one that works with signals with an unknown number of nonzero coefficients.

Algorithm 1 Reconstructing sparse signal with an unknown number of nonzero coefficients

Input: L observations $f = Pg$ (2.3)
Output: Reconstruction of sparse vector $\hat{g}$
$k = 0$
while Assumed number of nonzero coefficients $k \leqslant \dfrac{L}{2}$ and error decrease detector **do**
    $k = k + 1$
    Reconstruct k-sparse signal $\hat{g} = \sum_{r=1}^{k} \hat{a}_r \delta(n - \hat{n}_r)$ from f using finite-dimensional FRI technique
    Resynthesize observations $f_k = P\hat{g}$
    Compute error $\epsilon_k = \|f_k - f\|_2$
    if $k > 1$ **then**
        error decrease detector $=(\epsilon_k - \epsilon_{k-1}) < 0$
    end if
end while
$R_1 = k - 1$
Choose the signal $\hat{g}$ that corresponding to the model $\sum_{r=1}^{R_1} \hat{a}_r \delta(n - \hat{n}_r)$.

The idea behind the proposed reconstruction scheme is as follows. The available observations $\{f[l]\}_{l=0}^{L-1}$ provide at most $L/2$ nonzero coefficients. Let us initially assume that the number of nonzero coefficients is $k = 1$ and corresponding k-sparse signal $\sum_{r=1}^{k} \hat{a}_r \delta(n - \hat{n}_r)$ is reconstructed using finite-dimensional FRI technique. The reconstruction process operates in five steps.

1 Estimate annihilating filter q.

Consider filter q with $k+1$ components $\{q[l]\}_{l=0}^{k}$ whose transfer function has k zeros at η_r, that is, $Q(z) = \prod_{r=1}^{k}(1 - \eta_r z^{-1})$. It explicitly follows that

$$f[l] \star q[l] = \sum_{i=0}^{k} q[i] f[l-i] = 0. \tag{2.4}$$

The filter $q[l]$ is called annihilating filter because it annihilates the sequence $f[l]$. The corresponding matrix notation for (2.4) is given by

$$\begin{bmatrix} f[k] & f[k-1] & \dots & f[0] \\ f[k+1] & f[k] & \dots & f[1] \\ \vdots & \vdots & & \vdots \\ f[L-1] & f[L-2] & \dots & f[L-k-1] \end{bmatrix} \begin{bmatrix} q[0] \\ q[1] \\ \vdots \\ q[k] \end{bmatrix} = 0 = Fq, \tag{2.5}$$

where F is the Toeplitz matrix of size $(L-k) \times (k+1)$. This system yields a unique solution with the condition $q[0] = 1$ since the matrix F has rank k (Dragotti *et al.* 2007).

2 Compute solutions of underdetermined system (2.2).

$$g = P^H f + \sum_{t=1}^{T} \alpha_t s_t, \tag{2.6}$$

where P^H is the Hermitian matrix of P, $T = N - L$ is the dimension of null space of P, $\{s_t\}_{t=1}^{T}$ are null space basis of P and $\{\alpha_t\}_{t=1}^{T}$ are unknown values.

3 Find discrete Fourier transform of g.

Premultiplying (2.6) by unitary DFT matrix $U \in \mathbb{C}^{N \times N}$, we obtain DFT of g as

$$\hat{f} = Ug = UP^H f + \sum_{t=1}^{T} \alpha_t U s_t. \tag{2.7}$$

By defining $x = UP^H f$ and $Us_t = h_t$, equation (2.7) reduces to

$$\hat{f} = x + \sum_{t=1}^{T} \alpha_t h_t. \tag{2.8}$$

4 Determine unknown values $\{\alpha_t\}_{t=1}^{T}$.

Let $Tr\{.\}$ be an operator which maps $N \times 1$ vector $\hat{f}$ into an $(N-k) \times (k+1)$ Toeplitz matrix $\hat{F} = Tr\{\hat{f}\}$. Since N elements in vector $\hat{f}$ are of the form (2.3), the homogeneous system from (2.5) is also satisfied:

$$\hat{F}q = 0. \tag{2.9}$$

Substitute (2.8) in (2.9) to generate new linear system with T unknowns

$$\begin{bmatrix} H_1 q & H_2 q & \dots & H_T q \end{bmatrix} \begin{bmatrix} \alpha_1 \\ \alpha_2 \\ \vdots \\ \alpha_T \end{bmatrix} = -Xq, \tag{2.10}$$

where $X = Tr\{x\}$ and $H_t = Tr\{h_t\}$. This is an overdetermined system, and since q is known, which yields a unique solution (Oñativia *et al.* 2014).

5 Build k-sparse signal.

From the estimated values $\{\alpha_t\}_{t=1}^{T}$ and available observations f, we build k-sparse vector using equation (2.6).

Once k-sparse signal is reconstructed, we then resynthesize observations to obtain f_k and compute error on resynthesized observations with respect to the original observations, i.e $\epsilon_k = \|f_k - f\|_2$. Repeat the same procedure, however, with assumption that k is 2,3, until resynthesized error increases or same as previous, i.e $(\epsilon_k - \epsilon_{k-1}) \geq 0$ detected. The stopping number k gives the number of nonzero coefficients in the reconstructing signal and it is denoted by R_1. Finally, the problem is solved by choosing signal that corresponds to the model $\sum_{r=1}^{R_1} \hat{a}_r \delta(n - \hat{n}_r)$. The proposed scheme is summarized in Algorithm 1.

2.2.2 Reconstruction of sparse signal in presence of noise

Any practical acquisition device introduces noise during acquisition. As a result, we access the noisy observations

$$f'[l] \;=\; f[l] + v[l], \tag{2.11}$$

where $f[l]$ are noiseless observations and $v[l]$ are noise observations. From (2.3), the noisy observations $f'[l]$ can be written as

$$f'[l] \;=\; \frac{1}{\sqrt{N}} \sum_{r=1}^{R} a_r \eta_r^l + v[l], \tag{2.12}$$

with $l = 0, ..., L-1$ and where $\eta_r = e^{-j2\pi n_r/N}$.

Algorithm 2 Cadzow denoising method for noisy observations

1: **Input:** L noisy observations $f'[l]$.
2: **Output:** Denoised observations.
3: Construct square Toeplitz matrix Y from noisy observations $f'[l]$.
4: Perform SVD of $Y = ACB^H$.
5: Build matrix C'' from C by keeping k largest diagonal entries and zero elsewhere.
6: Update Y to its rank k approximation $Y = AC''B^H$.
7: Update Y to its Toeplitz approximation by averaging diagonals of Y.
8: Check the matrix Y whether it is rank deficient or not.
9: Repeat 4, 5, 6 and 7 until the matrix Y ceases to rank deficient.

Consequently, in a noisy environment, (2.5) is no longer satisfied since $F' = F + V$ where V is Toeplitz matrix with entries $v[l]$. However, the system (2.5) yields an approximate solution applying SVD to F'. The eigenvector corresponding to the minimum eigenvalue is the desired solution of annihilating filter q which is total least square (TLS) solution to (2.5). Once the filter q is known, the task is to estimate unknown values $\{\alpha_t\}_{t=1}^{T}$. In the noisy situation, (2.10) is not satisfied anymore since the system (2.5) does not hold exactly. Estimating the TLS solution allows us to resolve this issue as well. From estimated unknowns $\{\alpha_t\}_{t=1}^{T}$ and available observations f', build Fourier vector $\hat{f}'$ using (2.7) and employ Cadzow technique to $\hat{f}'$. Then, the k-sparse vector is obtained by taking inverse DFT of $\hat{f}'$. Using reconstructed $k-$sparse vector, resynthesized error ϵ_k is calculated. The procedure is repeated until error increases. Finally, the issue is resolved by selecting a signal based on stopping number k. Performance of the proposed reconstruction method can be improved by initial denoising before applying TLS using Cadzow's iterative technique. Main idea behind the Cadzow method is to build rank deficient matrix from the full rank matrix F' and is summarized in Algorithm 2.

2.3 Simulation results

2.3.1 Performance of universal scheme in absence of noise

Input in this experiment is a sparse signal with $R = 10$, $N = 256$ where nonzero positions $\{t_r\}_{r=1}^{R}$ and intensity values $\{a_r\}_{r=1}^{R}$ are chosen randomly between [1 256] and [3 5], respectively. The partial unitary DFT matrix used for obtaining observations is of size 20×256 which yields $L = 2R = 20$ observations (critical number of observations).

The proposed universal FRI scheme is employed on these observations to reconstruct the input signal. In Fig. 2.1(a), original and reconstructed sparse signals are plotted together, while in Fig. 2.1(b) observations taken by a partial unitary DFT matrix are given. We observe that reconstruction is perfect to numerical precision. In Fig. 2.2, even though number of observations changes from $L = 20$ to 40, perfect reconstruction still be achieved.

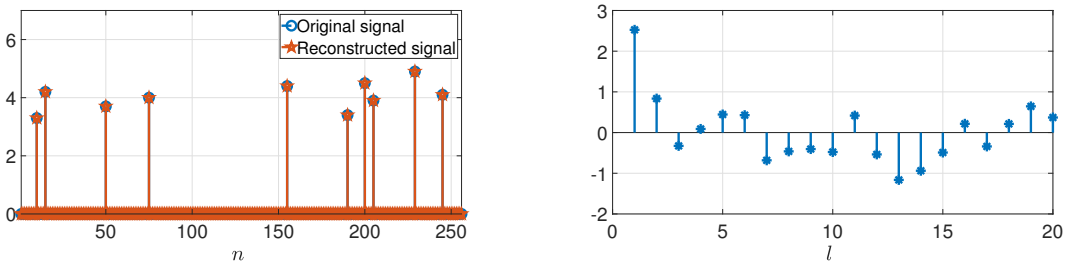

(a) (b)

Figure 2.1: (a) Original and reconstructed signal, and (b) available L=20 observations. Vertical: amplitude; Horizontal: index.

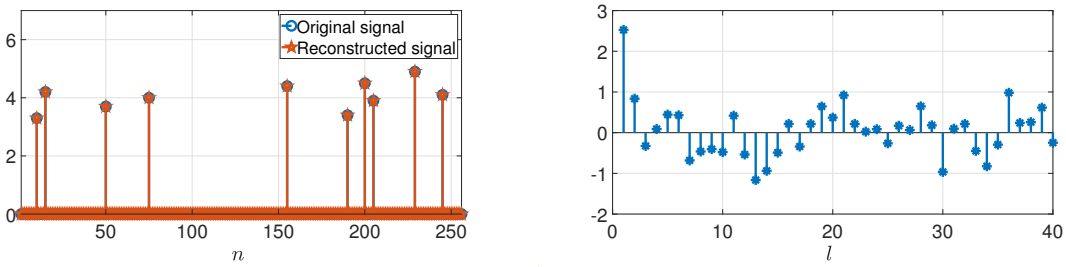

(a) (b)

Figure 2.2: (a) Original and reconstructed signal, and (b) available L=40 observations. Vertical: amplitude; Horizontal: index.

Fig. 2.3 shows average MSE of FRI (universal and traditional) and compressed sensing schemes (orthogonal matching pursuit (OMP) (Tropp and Gilbert 2007), approximate message passing (AMP) (Donoho *et al.* 2009), least angle regression (LARS) (Donoho and Tsaig 2008), total variation (TV) minimization (Cai *et al.* 2010)) over 100 random sparse signals w.r.t the number of observations. When number of observations is lesser than the threshold i.e $L = 140$, compressed sensing schemes are failed to reconstruct the sparse signals perfectly since the observations are consecutive. Therefore, universal and traditional FRI schemes are considered for rest of the

simulations as it gives perfect reconstructions even at critical number of observations i.e $L = 20$.

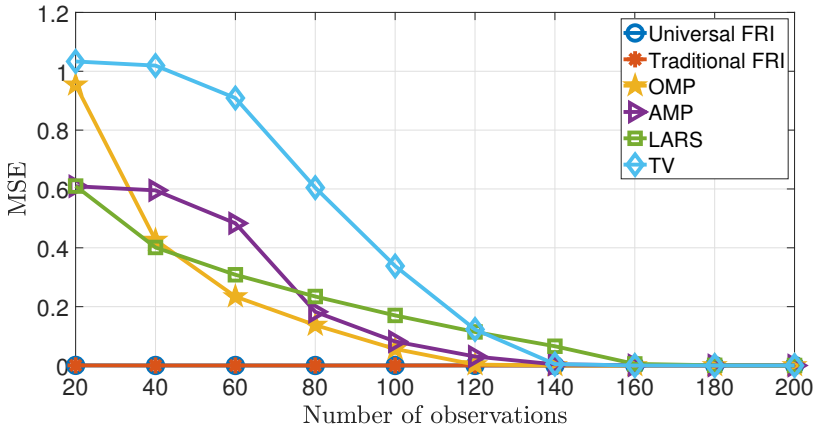

Figure 2.3: Average MSE of FRI and compressed sensing schemes w.r.t the number of observations.

2.3.2 Performance of universal scheme in presence of noise

In this scenario, an exact reconstruction of the sparse signal is not possible. In order to achieve reasonable reconstruction, number of observations must be increased, and denoising preprocessing is required as described in Section 2.2.2.

Two experiments are simulated to evaluate performance of the universal FRI scheme in presence of noise. In the first experiment, input signal is a sparse sequence of the form shown in (2.1) with R =10, N =256. The nonzero positions $\{t_r\}_{r=1}^{R}$ are chosen uniformly between [25 250] with a step of 25 and assume constant amplitudes with $\{a_r\}_{r=1}^{R} = 3$. The signal is contaminated by i.i.d Gaussian noise with zero mean and standard deviation σ. The standard deviation is chosen according to the SNR defined to be SNR (dB) = 10 $log\frac{\|g\|^2}{N\sigma^2}$. Measured L= 110, 125, 140, 155, 170, 185, and 200 observations of the signal and corresponding missing observations percentages are 57%, 51%, 45%, 39%, 33%, 27%, and 21%, respectively. To reconstruct input signal, following schemes are employed: (1) proposed scheme + Cadzow denoising, referred to as Universal FRI, and (2) traditional scheme + Cadzow denoising, referred to as Traditional FRI. We denoise the observations by applying 5 iterations of the Cadzow algorithm. SNR is varied from 2 dB to 20 dB in step size of 6 dB. Reconstruction performances of these schemes are compared in terms of average mean squared error

(MSE) calculated over 100 realizations for each noise level. MSE of the retrieved signal is computed as

$$MSE = \frac{1}{N}\sum_{n=1}^{N}\left(g[n] - \hat{g}[n]\right)^2, \tag{2.13}$$

where $g[n]$ is original signal and $\hat{g}[n]$ is reconstructed signal.

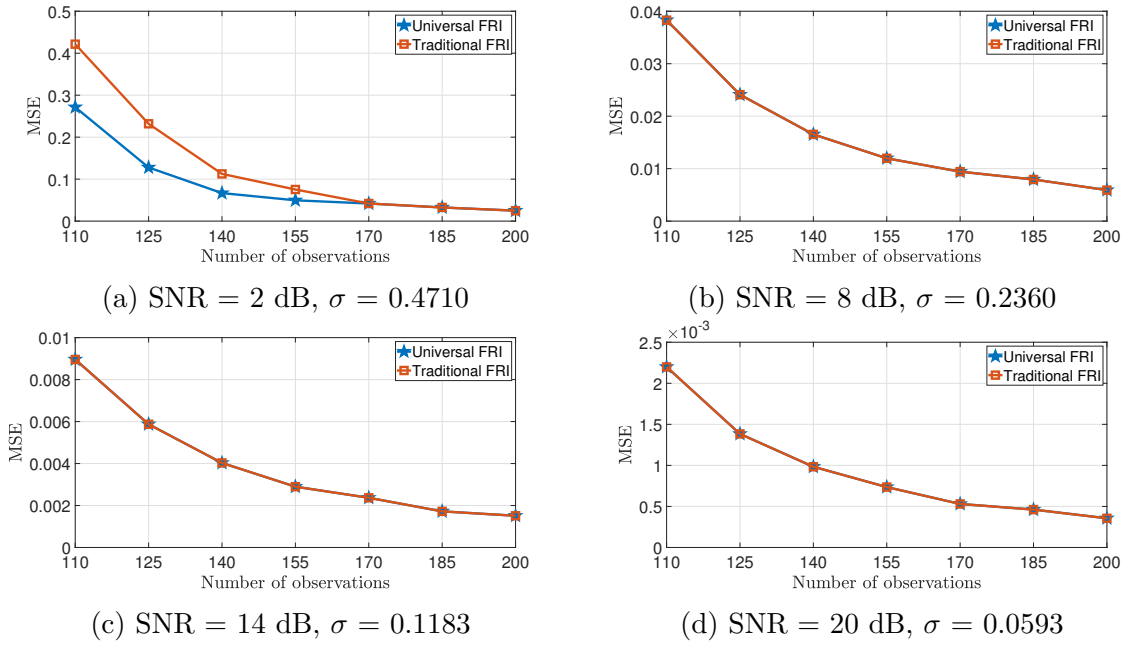

Figure 2.4: Average MSE of the proposed and the traditional schemes w.r.t number of observations at different levels of noise.

Plots in Fig. 2.4 show average MSE in reconstruction of the input signal w.r.t the number of observations L at various noise levels. In both schemes (proposed and the traditional), reconstruction accuracy is improved (MSE decreased) when SNR is increased from 2 dB to 20 dB, irrespective of the number of observations. The plots also illustrates that when the number of observations increases, reconstruction accuracy is also improved, irrespective of the SNR. The reason is that when number of observations is increased, the missing observations percentage decreases and hence improved the reconstruction accuracy. Moreover, from Fig. 2.4(b), 2.4(c), and 2.4(d), it is clear that proposed and the traditional schemes achieve optimal and similar performance at an SNR of 8 dB, 14 dB, and 20 dB, respectively. Performance of both schemes breaks down at 2 dB SNR. This is due to replacing location of the weakest signal subspace eigenvalue in SVD of noisy square Toeplitz matrix with orthogonal

subspace eigenvalues (subspace swap).

An expression relating breakdown standard deviation σ to the number of observations L has been presented in (Wei and Dragotti 2015)

$$\sigma > \frac{c_R}{\sqrt{\left(\frac{L+1}{2}\right) ln \left(\frac{L+1}{2}\right)}}, \qquad L \geq 2, \tag{2.14}$$

where c_R is the R^{th} singular value (weakest singular value of signal) in SVD of F. Fig. 2.5(a) shows breakdown condition as given in equation (2.14). The breakdown happens in the area above the curve. Since the standard deviation corresponding to 2 dB SNR (i.e σ =0.4710) lies above the curve, and therefore it is guaranteed to breakdown. At this breakdown, as the number of observations L goes down from 170, a significant improvement in performance (as MSE is small) is observed in the proposed scheme over the traditional scheme. This is because, universal scheme selects signal that corresponds to the minimum average error ϵ_k which contains lesser subspace swap as evident from Fig. 2.6 and 2.7. Whereas, at L= 170, 185, and 200, the traditional and proposed schemes perform similarly since the minimum average error ϵ_k occurred at the original number of nonzero coefficients (after that error ϵ_k increases).

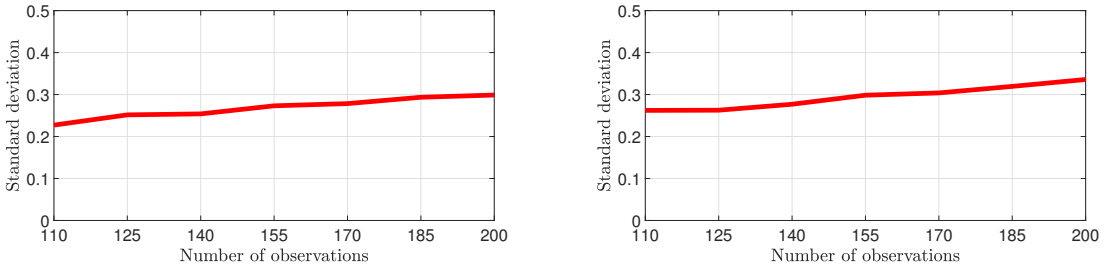

(a) (b)

Figure 2.5: Relationship between breakdown standard deviation and number of observations. (a) Uniform scenario (first experiment), and (b) random scenario (second experiment).

In the second experiment, R=10 nonzero positions $\{t_r\}_{r=1}^{R}$ and intensity values $\{a_r\}_{r=1}^{R}$ are chosen randomly between [1 256] and [3 5], respectively. Plots in the first column of Fig. 2.8 show average MSE w.r.t the number of observations at 2 dB, 8 dB, 14 dB, and 20 dB SNR. From Fig. 2.5(b), it is clear that performance of the traditional and proposed schemes breaks down at 2 dB and 8 dB SNR since corresponding σ= 0.6385, 0.3200 values lies above the curve. In this breakdown, they achieve similar

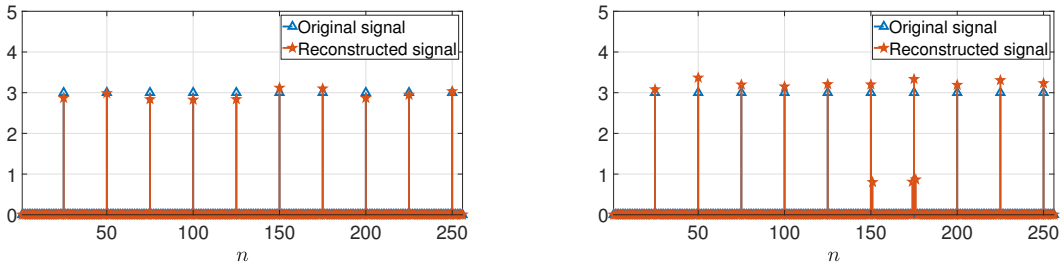

(a) (b)

Figure 2.6: Number of observations L=155, SNR=2 dB. (a) Original signal and reconstructed signal using universal scheme, and (b) original signal and reconstructed signal using traditional scheme. Vertical: amplitude; Horizontal: index.

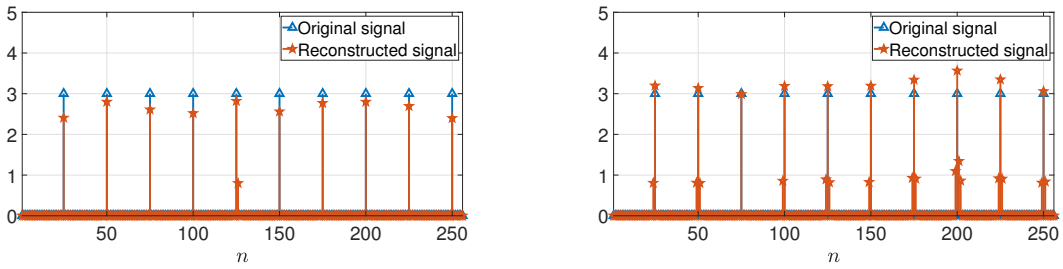

(a) (b)

Figure 2.7: Number of observations L=140, SNR=2 dB. (a) Original signal and reconstructed signal using universal scheme, and (b) original signal and reconstructed signal using traditional scheme. Vertical: amplitude; Horizontal: index.

performance at 8 dB, 14 dB, and 20 dB SNR, whereas, at 2 dB SNR, as the number of observations decreases, a significant improvement in performance is observed in the proposed scheme over the traditional scheme. Finally, these results clearly suggest that the proposed scheme outperforms the traditional scheme especially in smaller breakdown SNRs and in the case with less number of observations.

2.3.3 Time complexity of universal scheme

Plots in the second column of Fig. 2.8 shows average computational time (seconds) corresponding to the second experiment. At 8 dB, 14 dB, and 20 dB SNR, as the number of observations decreases, computational time of the proposed scheme is approximately constant and quite high as compared to traditional. The reason is iterative and minimum average error ϵ_k occurred at the original number of nonzero coefficients. Moreover, we observe that as the number of observations decreases, computational

time of the proposed scheme is reduced at an SNR of 2 dB. This is because, when the number of observations are decreased, the minimum average error ϵ_k has occurred at a lesser number of nonzero coefficients than the original number and hence computational time is decreased. Finally, these results suggest that the proposed scheme is slower than traditional scheme.

2.4 Applications of universal FRI scheme

2.4.1 Sampling and reconstruction of MR image

Reducing scan time is critical in MR imaging considering safety of patients. This encourages reconstructing clinically acceptable MR images using lesser sampling measurements. Compressive sensing techniques are commonly employed to reconstruct MR images using fewer measurements taken by either radial or Cartesian sampling scheme (Lustig *et al.* 2008, Chauffert *et al.* 2013, Feng *et al.* 2014). In radial sampling scheme, the signal is sampled along spokes instead of parallel rows and it has several advantageous over Cartesian scheme. While in Cartesian scheme a reduction of data lines tends to occurrence of aliasing effects that makes the image unusable, in radial scheme, majority of object information legible even for a significant number of streaking artefacts (Block 2008). Because of this, radial sampling is a particularly promising scheme for applications where it is crucial to acquire images quickly and where the diagnosis information is unaffected by tiny streaking patterns.

However, compressive sensing techniques suffer from slower convergence and they achieve better reconstruction only when observations are chosen at random. Due to hardware constraints, choosing random observations in MR imaging is not feasible. As a result, Prony's method (Vetterli *et al.* 2002) is employed to reconstruct MR images (Deslauriers-Gauthier and Marziliano 2011*b*), however, Prony's method requires computing polynomial roots of annihilating filter and this fact may lead to an unstable reconstruction in small SNRs. Alternatively, (Sudhakar Reddy *et al.* 2021) proposed a finite-dimensional FRI technique (a.k.a null space based FRI technique) (Oñativia *et al.* 2014) to reconstruct MR images which avoids root finding step. These are not universal in the perspective that the knowledge of L0 norm is required for reconstruction. To address this problem, we employed universal FRI scheme as discussed in Section 2.2.

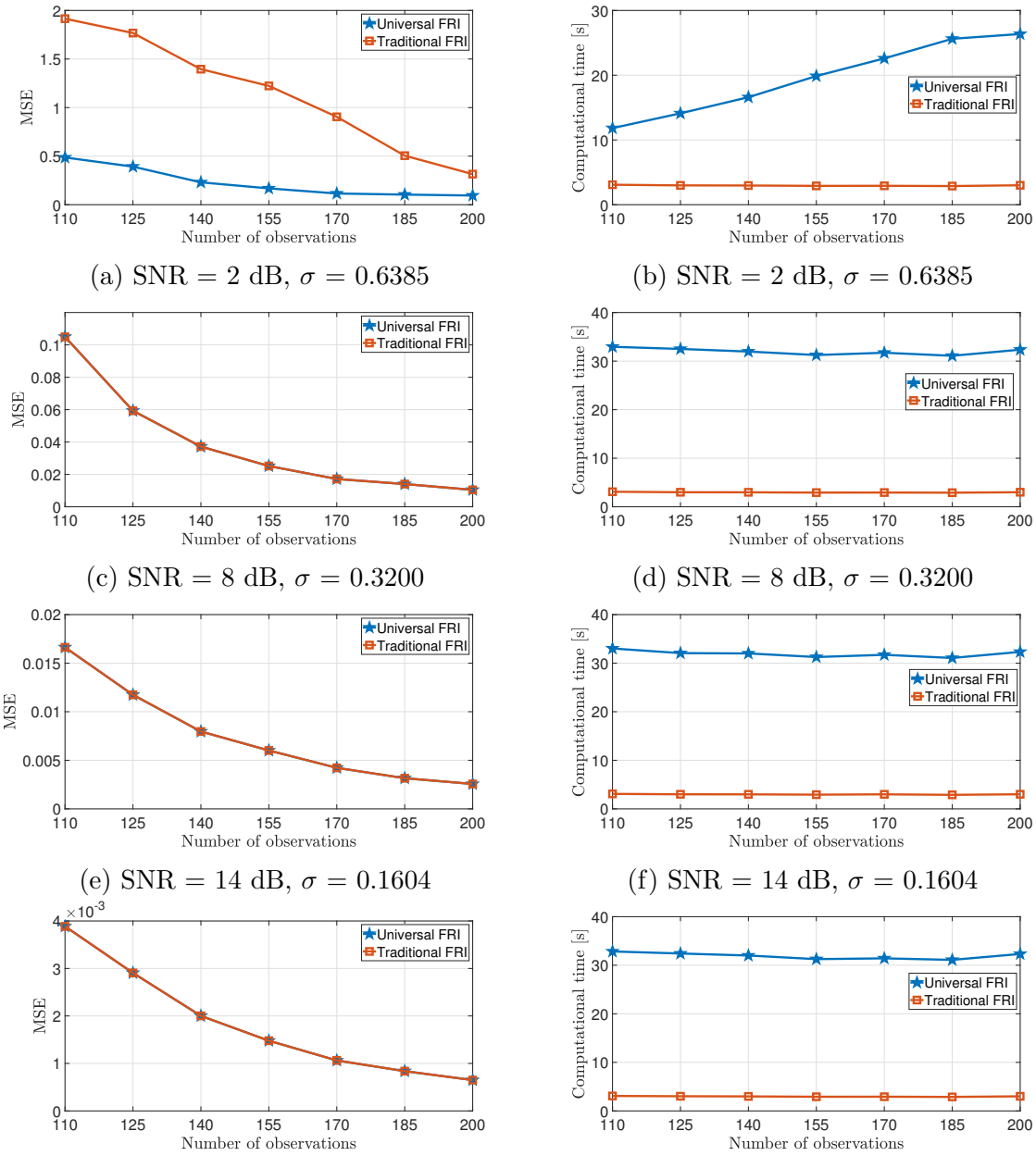

(a) SNR = 2 dB, $\sigma = 0.6385$

(b) SNR = 2 dB, $\sigma = 0.6385$

(c) SNR = 8 dB, $\sigma = 0.3200$

(d) SNR = 8 dB, $\sigma = 0.3200$

(e) SNR = 14 dB, $\sigma = 0.1604$

(f) SNR = 14 dB, $\sigma = 0.1604$

(g) SNR = 20 dB, $\sigma = 0.0804$

(h) SNR = 20 dB, $\sigma = 0.0804$

Figure 2.8: Average MSE and computational time of the proposed and traditional schemes w.r.t the number of observations at different levels of noise.

In MR imaging, sampling and reconstruction process operate in four steps. MR image is the concatenation of a set of S column vectors $\{h_i\}_{i=1}^{S}$. The first step is a finite-difference operation applied to each column vector of the MR image which

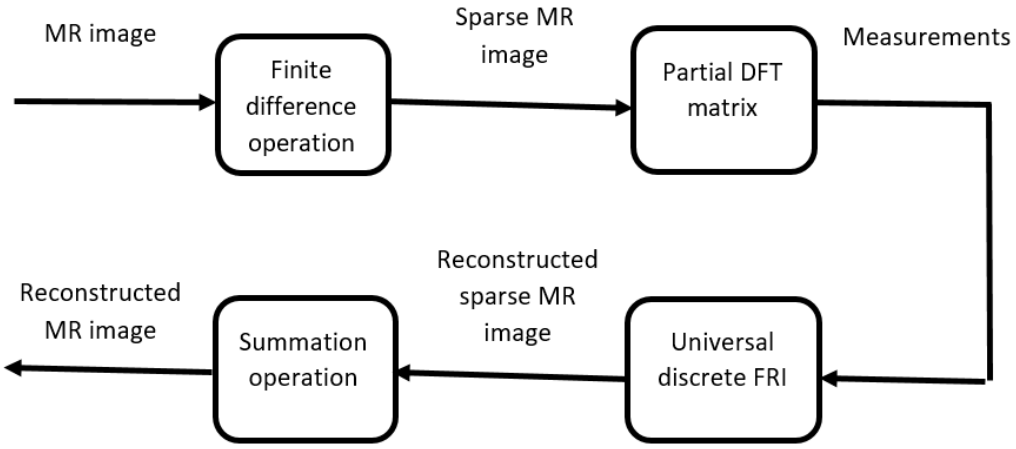

Figure 2.9: Block diagram of sampling and reconstruction of MR image.

generates a set of S sparse vectors $\{g_i\}_{i=1}^{S}$, i.e,

$$g_i[n] = h_i[n] - h_i[n-1], \qquad n = 1, 2, ..., N-1, \tag{2.15}$$

where $g_i[0] = h_i[0]$. The second step is multiplying each sparse vector with a partial unitary DFT matrix $(P)_{l\times n} = e^{-j2\pi ln/N}/\sqrt{N}$ with $l = 0, 1, 2, ..., L-1$ and $n = 0, 1, 2, ..., N-1$ $(L < N)$ which is obtained by removing last $N - L$ rows of full DFT matrix $(P)_{l\times n} = e^{-j2\pi ln/N}/\sqrt{N}$ with $l = 0, 1, 2, ..., N-1$ and $n = 0, 1, 2, ..., N-1$ leads to a set of S measurement vectors $\{f_i\}_{i=1}^{S}$

$$f_i[l] \;=\; \frac{1}{\sqrt{N}} \sum_{n=0}^{N-1} g_i[n] e^{-j2\pi nl/N}, \qquad l = 0, 1, 2, ..., L-1. \tag{2.16}$$

The third step results in S measurement vectors $\{f_i\}_{i=1}^{S}$ which are input to the proposed scheme, we then retrieve the set of S sparse vectors $\{\hat{g}_i\}_{i=1}^{S}$. Finally, a summation operation is applied to each reconstructed sparse vector $\{\hat{g}_i\}_{i=1}^{S}$ to obtain the MR image $\{\hat{h}_i\}_{i=1}^{S}$ i.e

$$\hat{h}_i[n] = \sum_{q=1}^{n} \hat{g}_i[q], \tag{2.17}$$

for $n = 0, 1, 2, ..., N-1$ and $i = 1, 2, ..., S$. Fig. 2.9 depicts schematic block diagram of sampling and reconstruction of MR image.

2.4.2 Sampling and reconstruction of QRS complex

Bio-signals utilised for tracking and identifying different cardiac problems include ECG signals. In particular, QRS complexes are crucial for medical diagnoses and therapies. Due to their particular shape, Hermite transform is determined to be useful for sparse representation of QRS complexes (Brajović *et al.* 2017, Stanković *et al.* 2019). Therefore, Hermite transform allows compression of ECG signals. However, authors proposed compressive sensing techniques for signal reconstruction from lesser measurements. In MR image reconstruction, we have already discussed drawbacks of these techniques. To overcome those problems, universal FRI is employed to reconstruct QRS complexes.

Sampling and reconstruction of QRS complexes also operates in four steps. The first step is Hermite transform applied to QRS complex h which generates a sparse signal g, i.e,

$$g[n] = \frac{1}{N}\sum_{i=1}^{N}\frac{\Upsilon_n(t_i)}{[\Upsilon_{N-1}(t_i)]^2}h(t_i), \qquad n = 0, 1, 2, ..., N-1, \tag{2.18}$$

where $\Upsilon_0(t_i) = \frac{1}{\sqrt[4]{\pi}}e^{-\frac{t_i^2}{2}}$, $\Upsilon_1(t_i) = \frac{\sqrt{2}t_i}{\sqrt[4]{\pi}}e^{-\frac{t_i^2}{2}}$, $\Upsilon_n(t_i) = t_i\sqrt{\frac{2}{n}}\Upsilon_{n-1}(t_i) - \sqrt{\frac{n-1}{n}}\Upsilon_{n-2}(t_i)$ $n > 2$. For further information of the Hermite transform see (Stanković *et al.* 2019). The second step is multiplying sparse signal g with a matrix $(P)_{l\times n} = e^{-j2\pi ln/N}/\sqrt{N}$ with $l = 0, 1, 2, ..., L-1$ and $n = 0, 1, 2, ..., N-1$ $(L < N)$ which leads to measurement signal f

$$f[l] \;=\; \frac{1}{\sqrt{N}}\sum_{n=0}^{N-1} g[n]e^{-j2\pi nl/N}, \qquad l = 0, 1, 2, ..., L-1. \tag{2.19}$$

The third step is to retrieve the sparse signal $\hat{g}$ from acquired measurement signal f by employing the proposed scheme. Finally, inverse Hermite transform is used to reconstruct the QRS complex $\hat{h}$ from the reconstructed sparse signal.

2.4.3 Performance of universal scheme in absence of noise

In the case of MR imaging, generally, Shepp-Logan phantom is simulated to evaluate performance of the proposed scheme. Starting with the Shepp-Logan phantom image

with a resolution of 256×256 is considered (see Fig. 2.10(a)), which is the concatenation of $S = 256$ column vectors. A finite-difference operation is applied to every column vector which results in sparse image as shown in Fig. 2.10(b).

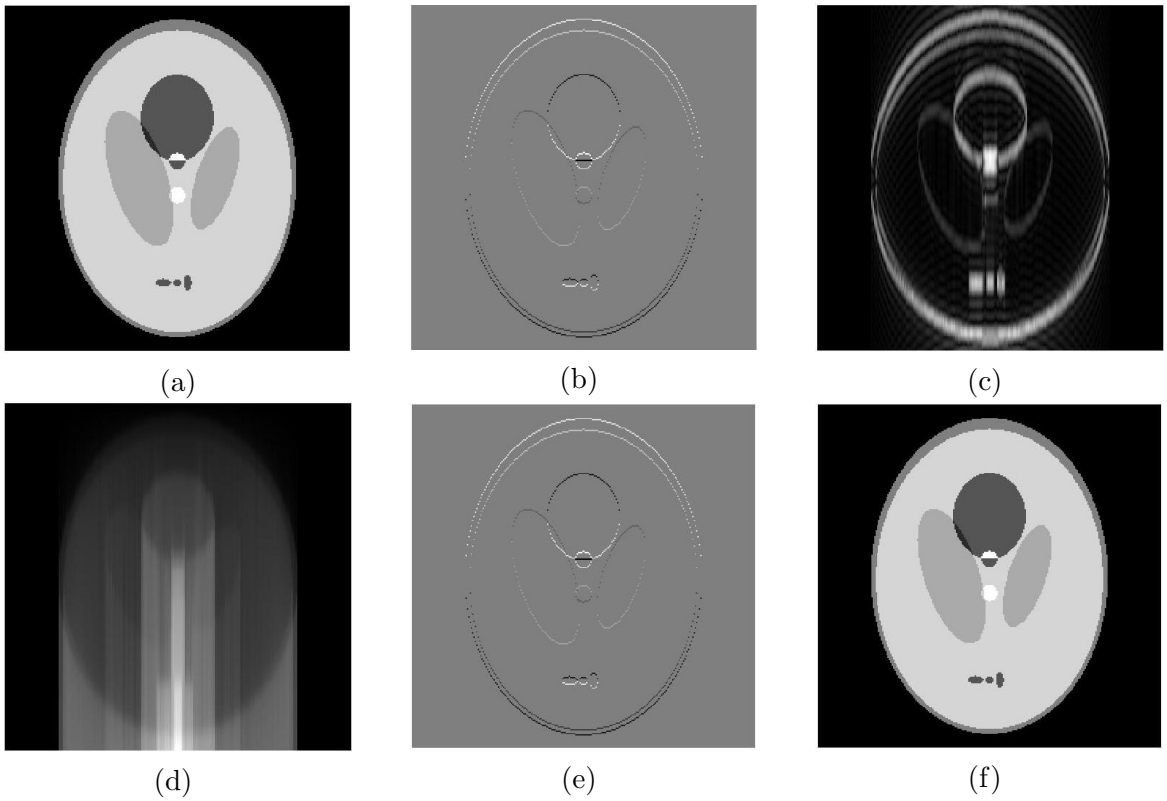

Figure 2.10: (a) Shepp-Logan phantom with a resolution of 256×256. (b) Finite difference of the phantom (sparse image). (c) Aliased sparse image. (d) Aliased phantom image. (e) Reconstructed sparse image. (f) Reconstructed phantom image.

Measured $L = 28$ observations for each sparse vector with partial unitary DFT matrix P of size 28×256 since a maximum of 14 nonzero coefficients is obtained for each vector. Resulting aliased images of size 256×256 are shown in Fig. 2.10(c) and 2.10(d). Then, the proposed universal FRI scheme is employed to all measurement vectors to reconstruct sparse image and subsequently applied summation operation to get back the MR image. Reconstructed sparse and MR image are shown in Fig. 2.10(e) and 2.10(f), respectively. MSE of reconstructed MR image is 1.7921×10^{-19}.

In the case of QRS complex, QRS complexes are isolated from the real ECG signal, and Fig. 2.11(a) displays the time domain interpretation of one of its QRS complexes with signal length $N = 51$. To attain sparsity, Hermite transform is employed and sparse coefficients are depicted in Fig. 2.11(b). Measured $L = 20$ observations since

10 nonzero Hermite transform coefficients is obtained. The available observations are depicted in Fig. 2.11(c). Then, reconstruction of QRS complex is performed using the proposed scheme. The reconstructed QRS complex is shown in Fig. 2.11(d). MSE of the reconstructed QRS complex is 6.5905 $\times 10^{-05}$. From these results, we infer that reconstruction of MR image and QRS complex is exact to a numerical precision.

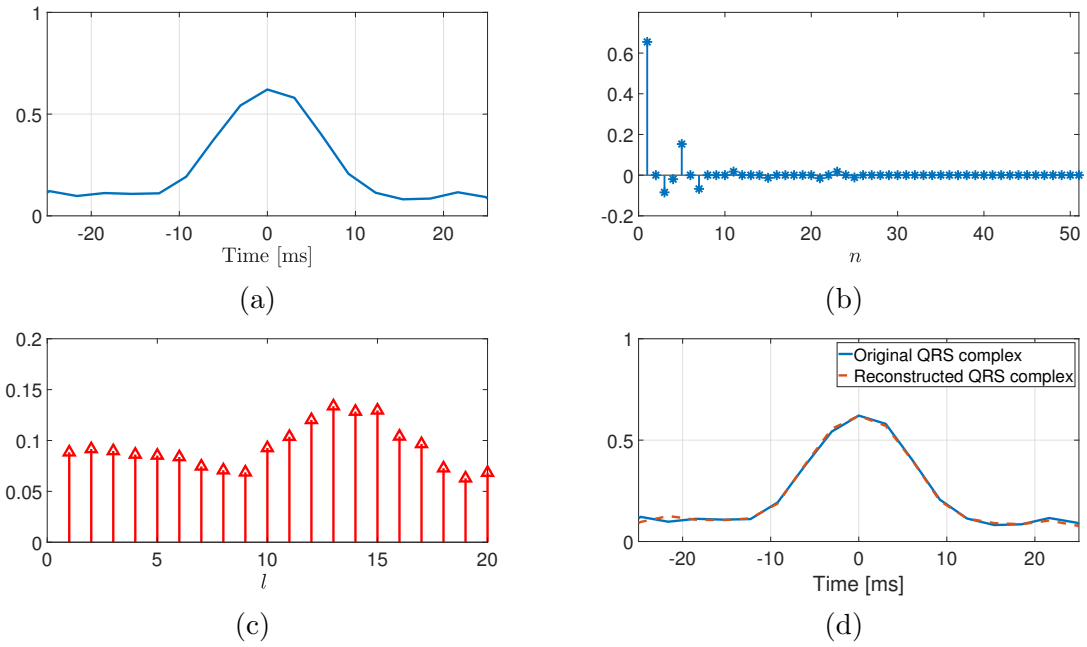

Figure 2.11: (a) QRS complex of the ECG signal. (b) Hermite transform of the QRS complex. (c) Measurements of the Hermite transform of the QRS complex. (d) Original and reconstructed QRS complex.

2.4.4 Performance of universal scheme in presence of noise

In practical scenario, as we know, observations are corrupted by noise, hence to evaluate performance of the algorithm, each sparse vector is contaminated by Gaussian noise with SNR levels 2 dB and 8 dB, respectively. Measured observations L= 170, 185, 200, 215, 230, and 245 for each sparse vector and corresponding percentages of missing observations are 33%, 27%, 21%, 15%, 9%, and 3%, respectively (in the case of QRS complex, we measured L= 35, 38, 41, 44, and 47 observations and corresponding missing observations are 31%, 25%, 19%, 13%, and 7%). To reconstruct input MR image and QRS complex, the proposed scheme with Cadzow denoising and traditional scheme with Cadzow denoising (Sudhakar Reddy *et al.* 2021) are employed. Experi-

ment is carried out with 100 realizations for each noise level, and average MSE of the MR image and QRS complex is given in Table 2.1 and Table 2.2, respectively.

Table 2.1: Average MSE of the traditional and universal schemes over 100 realizations w.r.t the number of observations at different noise levels (MR image).

	SNR=2 dB		SNR =8 dB	
L	Traditional	Universal	Traditional	Universal
170	0.2253	1.3922×10^{-4}	0.0027	1.1868×10^{-4}
185	0.1355	1.1360×10^{-4}	0.0018	1.0840×10^{-4}
200	0.0453	1.0884×10^{-4}	0.0014	9.9704×10^{-5}
215	0.0355	9.1640×10^{-5}	0.0011	9.8608×10^{-5}
230	0.0017	8.2839×10^{-5}	9.6244×10^{-4}	9.5281×10^{-5}
245	0.0015	7.4469×10^{-5}	8.8771×10^{-4}	7.9471×10^{-5}

Tables 2.1 and 2.2 show that when the noise level drops from 8 dB to 2 dB, the universal method performs significantly better at reconstruction than the traditional approach. In addition, we also observe that reconstruction performance is improved with increase in the number of observations L, which results improve the quality of the image as evident from Fig. 2.12, 2.13, and 2.14. Moreover, the results indicate that the proposed scheme has superior reconstruction accuracy than the traditional scheme especially in smaller SNR values and with a lesser number of observations.

Table 2.2: Average MSE of the traditional and universal schemes over 100 realizations w.r.t the number of observations at different noise levels (QRS complex).

	SNR=2 dB		SNR =8 dB	
L	Traditional	Universal	Traditional	Universal
35	0.4811	0.0040	0.2901	0.0031
38	0.2340	0.0036	0.1503	0.0022
41	0.1011	0.0033	0.0892	0.0019
44	0.0302	0.0031	0.0059	0.0018
47	0.0088	0.0029	0.0041	0.0015

(a) (b) MSE=0.0027 (c) MSE=1.1868×10^{-4}

Figure 2.12: Number of observations L=170, SNR=8 dB. (a) Original Shepp-Logan phantom image, (b) reconstructed phantom image using traditional scheme, and (c) reconstructed phantom image using universal scheme.

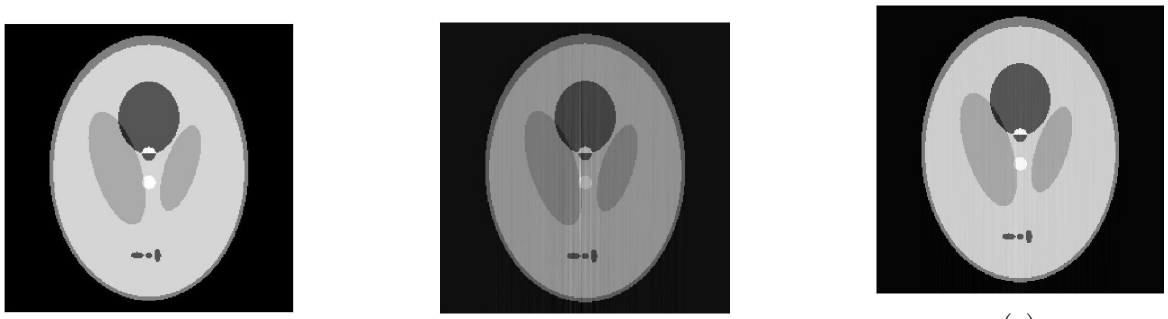

(a) (b) MSE=0.0014 (c) MSE=9.9704×10^{-5}

Figure 2.13: Number of observations L=200, SNR=8 dB. (a) Original Shepp-Logan phantom image, (b) reconstructed phantom image using traditional scheme, and (c) reconstructed phantom image using universal scheme.

(a) (b) MSE=9.6244×10^{-4} (c) MSE=9.5281×10^{-5}

Figure 2.14: Number of observations L=230, SNR=8 dB. (a) Original Shepp-Logan phantom image, (b) reconstructed phantom image using traditional scheme, and (c) reconstructed phantom image using universal scheme.

2.5 Summary

In this chapter, we have shown a universal FRI scheme based on the error reduction detector criterion that makes it possible to reconstruct sparse signals with an unknown number of nonzero coefficients. Furthermore, an application of the universal FRI on MR imaging and ECG is demonstrated. The effectiveness of the proposed scheme has been verified by simulation results.

Chapter 3

SPARSE-PRONY AND RESIDUAL NEURAL NETWORK FOR FRI SIGNAL RECONSTRUCTION

3.1 Introduction

The traditional finite rate of innovation (FRI) algorithms such as Prony's (Blu *et al.* 2008) and matrix pencil methods (Urigüen *et al.* 2013) are based on the singular value decomposition (SVD). The subspace strategy decomposes the measurement space into a signal subspace and an orthogonal subspace. (Blu *et al.* 2008, Urigüen *et al.* 2013, Leung *et al.* 2020) demonstrate that these algorithms achieve optimal results up to a certain signal-to-noise ratio (SNR) and worsen when the SNR falls below a certain threshold. Reason for the same is the occurrence of subspace swap wherein there may occur interchange of signal and orthogonal subspaces under noisy conditions (Wei and Dragotti 2015, 2017). Moreover, Prony's method makes use of an annihilating filter which requires to solve polynomial roots. Due to this, reconstruction accuracy may get degraded when signal samples are corrupted with noise.

In this chapter, we propose annihilating filter for reconstructing FRI signals based on sparsity of the amplitude parameters. The method does not require finding roots of the filter polynomial and refer to this approach as sparse-Prony method. The anni-

hilating filter is estimated from measurement samples. Analog time is quantized and the measurement vector is sparsely represented. The time delay and amplitude parameters are estimated by solving an optimization problem. Additionally, to overcome the subspace swap problem, a residual convolutional neural network approach, which estimates the signal parameters, is proposed. Network learns from the training data and gives the signal parameters from the discrete sample values. In the experimental setup, stream of Diracs is used as input signal, and exponential-reproducing kernel is considered for sampling. Simulation results are reported for noiseless and noisy cases to verify performance, and the proposed methods compared with the traditional methods and its robustness in the breakdown SNR is demonstrated. Further, the proposed sparse-Prony is extended to infer the times of action potentials from calcium imaging data.

The chapter is arranged as follows: Section 3.2 describes the proposed sparse-Prony method for noiseless and noisy scenarios. Section 3.3 describes the proposed residual convolutional neural network approach for noisy scenario. Section 3.4 presents simulation results of the proposed FRI methods and compares them with the traditional methods. Section 3.5 describes a method for spike train inference from calcium imaging data based on the proposed sparse-Prony method. Finally, summarize the chapter in Section 3.6.

3.2 Sparse-Prony method

In this section, we explain the proposed sparse-Prony method for reconstructing a stream of Diracs. Here, assumed exponential reproducing kernel as sampling kernel $\varphi(t)$ for obtaining measurement samples $f[n]$ and signal reconstruction from samples is considered separately for noisy and noiseless scenarios.

3.2.1 Reconstruction: In absence of noise

Assuming that the input $g(t)$ is a finite-length streams of Diracs

$$g(t) = \sum_{r=1}^{R} a_r \delta(t - t_r), \qquad t_r \in [0, \tau) \tag{3.1}$$

where τ is time length of the signal, R is number of Diracs, and $\{t_r, a_r\}_{r=1}^{R}$ correspond to time delays and amplitudes of R Diracs.

As given in the model of Fig. 1.1, signal $g(t)$ is filtered with an exponential reproducing kernel of $\varphi(t)$ (1.20) with $\alpha_l = j\omega_l = j(\omega_0 + l\lambda)$ and $l = 0, 1, ..., P$ and then uniformly sampled at intervals of time $t = nT$. The samples $f[n]$ is expressed as

$$f[n] = \left\langle g(t), \varphi\left(\frac{t}{T} - n\right)\right\rangle, \tag{3.2}$$

where $n = 1, 2, ..., N$ is the number of measurement samples and $N = \tau/T$ is the total number of measurement samples. Having obtained a set of measurement samples $f[n]$ as described above, the task is to reconstruct FRI signal $g(t)$ from the samples.

Signal, a stream of Diracs, is retrieved from a set of measurement samples $f[n]$ as follows:

1 First, we obtain new measurements $q[l]$ from the measurement samples $f[n]$. The $q[l]$, $l = 0, 1, ..., P$, is a linear combination of samples $f[n]$ (3.2) and coefficients $c_{l,n}$ (1.29) (Dragotti *et al.* 2007), and is represented as

$$\begin{aligned} q[l] = \sum_{n=1}^{N} c_{l,n} f[n] &= \sum_{n=1}^{N} c_{l,n} \left\langle g(t), \varphi\left(\frac{t}{T} - n\right)\right\rangle \\ &= \sum_{r=1}^{R} a_r e^{j\omega_l t_r/T} \\ &= \sum_{r=1}^{R} b_r \mu_r^l \end{aligned} \tag{3.3}$$

where $b_r = a_r e^{j\omega_0 t_r/T}$ and $\mu_r = e^{j\lambda t_r/T}$.

2 Then, estimate annihilating filter $\mathbf{d}$ with $R + 1$ coefficients $\{\mathbf{d}[l]\}_{l=0}^{R}$ having R zeros at μ_r in the transfer function $D(z) = \prod_{r=1}^{R}(1 - \mu_r z^{-1})$. As the $q[l]$ contains R complex exponentials μ_r, the $\mathbf{d}$ is an annihilating filter and satisfies the condition

$$q[l] \star \mathbf{d}[l] = \sum_{i=0}^{R} \mathbf{d}[i] q[l - i] = 0. \tag{3.4}$$

This is represented in a matrix form as

$$\begin{bmatrix} q[R] & \dots & q[1] & q[0] \\ q[R+1] & \dots & q[2] & q[1] \\ \vdots & & \vdots & \vdots \\ q[P] & \dots & q[P-R+1] & q[P-R] \end{bmatrix} \begin{bmatrix} \mathbf{d}[0] \\ \mathbf{d}[1] \\ \vdots \\ \mathbf{d}[R] \end{bmatrix} = 0 = Q\mathbf{d} \tag{3.5}$$

where Q is the Toeplitz matrix of size $(P-R+1)\times(R+1)$. The matrix Q is rank deficient with rank R if $P+1 \geq 2R$. The coefficient $\mathbf{d}[l]$ is estimated from (3.5) as null-space of Q with $\mathbf{d}[0]=1$ (Mulleti and Seelamantula 2015).

In the Prony's method, after knowing the annihilating filter $\mathbf{d}$, time delays are retrieved from roots of the filter (Vetterli *et al.* 2002, Dragotti *et al.* 2007). We propose an alternate approach which doesn't involve root-finding step, and is based on sparse representation of measurements $q[l]$ (Huang *et al.* 2016). In addition to steps 1 and 2, the proposed sparse-Prony method includes the following steps as explained.

3 Quantize the analog time with a resolution step of Δ as $t = k\Delta$ with $k = 0, 1, ..., K-1$ and $K = \tau/\Delta$ and unknown time delays t_r is approximated as $t_r = k_r\Delta$. Then (3.3) becomes

$$q[l] \;=\; \sum_{r=1}^{R} a_r e^{j\omega_l k_r \Delta/T}, \qquad l = 0, 1, ..., P, \tag{3.6}$$

where $k_r \in [0, K-1]$ is discrete value of time delays t_r. The (3.6) is isolated into $P-R+1$ sub problems

$$\begin{bmatrix} q[l] \\ q[l+1] \\ \vdots \\ q[l+R] \end{bmatrix} = \begin{bmatrix} e^{j\omega_l k_1\Delta/T} & e^{j\omega_l k_2\Delta/T} & \dots & e^{j\omega_l k_R\Delta/T} \\ e^{j\omega_{l+1} k_1\Delta/T} & e^{j\omega_{l+1} k_2\Delta/T} & \dots & e^{j\omega_{l+1} k_R\Delta/T} \\ \vdots & \vdots & & \vdots \\ e^{j\omega_{l+R} k_1\Delta/T} & e^{j\omega_{l+R} k_2\Delta/T} & \dots & e^{j\omega_{l+R} k_R\Delta/T} \end{bmatrix} \begin{bmatrix} a_1 \\ a_2 \\ \vdots \\ a_R \end{bmatrix} \tag{3.7}$$

where $l = 0, 1, ..., P-R$.

4 Take a set of analog time $S = \{0, \Delta, 2\Delta, ..., (K-1)\Delta\}$, and unknown time

delays $M = \{k_1\Delta, k_2\Delta, ..., k_R\Delta\}$, and $M \subset S$, then (3.7) is rewritten as

$$\begin{bmatrix} q[l] \\ q[l+1] \\ \vdots \\ q[l+R] \end{bmatrix} = \begin{bmatrix} 1 & e^{j\omega_l \Delta/T} & \dots & e^{j\omega_l (K-1)\Delta/T} \\ 1 & e^{j\omega_{l+1} \Delta/T} & \dots & e^{j\omega_{l+1} (K-1)\Delta/T} \\ \vdots & \vdots & & \vdots \\ 1 & e^{j\omega_{l+R} \Delta/T} & \dots & e^{j\omega_{l+R} (K-1)\Delta/T} \end{bmatrix} \begin{bmatrix} g_0 \\ g_1 \\ \vdots \\ g_{K-1} \end{bmatrix} \tag{3.8}$$

where $l = 0, 1, ..., P-R$ and $[g_0, g_1, ..., g_{K-1}]^T$ is a $K \times 1$ vector, formed by R amplitude parameters $\{a_r\}_{r=1}^R$ and $(K-R)$ zeros. This gives sparse representation of the measurement vector. Expression (3.8) is written as

$$\Lambda_l = B_l G \tag{3.9}$$

where $\Lambda_l = [q[l], q[l+1], ..., q[l+R]]^T \in \mathbb{C}^{(R+1)\times 1}$ is measurement vector, $B_l \in \mathbb{C}^{(R+1)\times K}$ is measurement matrix, $G = [g_0, g_1, ..., g_{K-1}]^T \in \mathbb{R}^{K\times 1}$ is an R-sparse vector with nonzero entries at indices $\{k_r\}_{r=1}^R$, and corresponding nonzero element values are $\{a_r\}_{r=1}^R$.

5 Next, time delay parameters of the Diracs are determined as described; from (3.5), $\mathbf{d}$ is orthogonal to Λ_l for any l which leads to

$$B_l^H \mathbf{d} = 0 \tag{3.10}$$

where $l = 0, 1, ..., P-R$ and superscript H denotes Hermitian transpose of a matrix. In a numerical implementation, multiplication in (3.10) does not produce exactly zero. The indices $\{k_r\}_{r=1}^R$ are estimated by choosing indices associated with R values that minimize $|B_l^H \mathbf{d}|$ (Deslauriers-Gauthier and Marziliano 2011*a*) where $|.|$ denotes absolute value. Once indices of nonzero entries of the vector G are found, time delays are directly calculated as $\hat{t}_r = k_r\Delta$.

6 Finally, amplitude parameters of the Diracs are determined as explained, amplitudes are estimated via $\hat{a}_r = B_R^+ \Lambda$, where B_R^+ is pseudoinverse of the matrix B_R. The B_R is obtained by keeping columns that correspond to the estimated indices $\{k_r\}_{r=1}^R$ in B_l.

To reconstruct the signal, time delay and amplitude parameters of these Diracs are

thus found. From these parameters, we reconstruct the signal $g(t)$ as

$$\hat{g}(t) = \sum_{r=1}^{R} \hat{a}_r \delta(t - \hat{t}_r) \tag{3.11}$$

3.2.2 Reconstruction: In presence of noise

Any signal-acquisition device introduces noise during measurement process. Therefore, we assume that instead of clean samples as in (3.2), we have access to noisy samples

$$\tilde{f}[n] = f[n] + \varepsilon[n] = \left\langle g(t), \varphi\left(\frac{t}{T} - n\right)\right\rangle + \varepsilon[n] \tag{3.12}$$

where $n = 1, 2, ..., N$ and where $\varepsilon[n]$ are i.i.d random samples from Gaussian distribution. When noise affects samples $f[n]$, noisy measurements from (3.3) becomes

$$\tilde{q}[l] = \sum_{n=1}^{N} c_{l,n} \tilde{f}[n] = \sum_{r=1}^{R} b_r \mu_r^l + s[l]. \tag{3.13}$$

for $l = 0, 1, ..., P$ and where $b_r = a_r e^{j\omega_0 t_r/T}$ and $\mu_r = e^{j\lambda t_r/T}$.

In the noisy case, (3.5) is not satisfied as $\tilde{Q} = Q + S$ where S is Toeplitz having entries $s[l]$ from (3.13). The (3.5) is approximately solved using SVD with more than critical number of measurements ($P+1 > 2R$). Estimate of $\mathbf{d}$ is obtained as the eigenvector corresponding to the smallest eigenvalue. We used Cadzow iterative algorithm to preprocessing the noisy measurements which inturn improves the estimate of $\mathbf{d}$.

3.3 Residual neural network approach

Deep-Learning is a part of machine learning which is developed from artificial neural networks. Even-though the research work on artificial neural networks started in 1940, the breakthrough came in the year 2012. Krizhevsky et al (Krizhevsky *et al.* 2012*a*) made way for the deep convolutional neural network and came up with the idea of adding more numbers of layers. After a while, there was a realization that, by going deeper, performance is not improved due to exploding/vanishing gradients. Deep learning has been explored using a variety of architectures. Since the past few

years, networks have gotten so deep that it has become very difficult to visualise the entire model. Prior to the residual neural network (ResNet) architecture (He *et al.* 2016) presented many architectures. Some of the important architectures are LeNet-5 (LeCun *et al.* 1998) with 60,000 parameters, AlexNet (Krizhevsky *et al.* 2012*b*) having 60M parameters and VGG16 (Simonyan and Zisserman 2014) with a large amount of 138M parameters.

3.3.1 ResNet-50

The ResNet-50 architecture mainly consists of two blocks i.e. identity block and a convolution block. The main difference between the two is a convolution layer in the shortcut path for convolution block but not for identity block. This architecture consists of five stages each with a convolution block and an identity block as shown in the Fig. 3.1. Each of convolution block and identity block consists of 3 convolutional layers. The model used is shown in Fig. 3.1 and is described as:

Zero-Pad: It pads the input with zeros of given size.
Stage 1: It contains a convolutional block of 50 filters with batch normalization followed by MaxPooling.
Stage 2: The convolutional block followed by two identity blocks with three sets of filters each.
Stage 3: The convolutional and identity blocks each uses three sets of filters.
Stage 4: It contains a convolutional block with three set of filters followed by 5 identity blocks which use three set of filters.
Stage 5: This is same as stage 3.

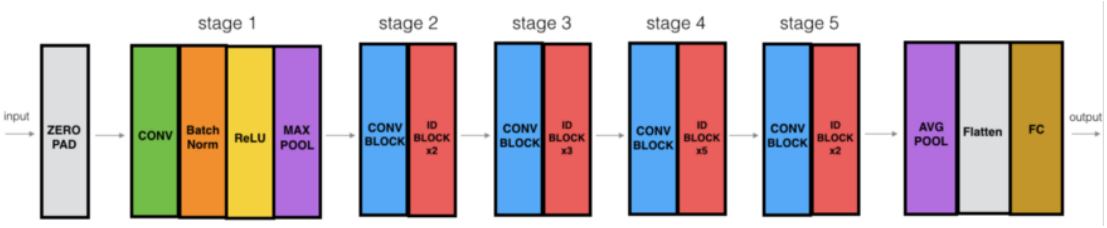

Figure 3.1: ResNet-50

The 1-D Average Pooling uses a shape 2 window. The flatten does not have any hyperparameters. The model uses dropout regularization. The Fully Connected (Dense) layer by using a softmax activation function reduces its input to the required number

of classes.

3.3.2 Reconstruction: In presence of noise

The occurrence of the larger magnitudes of the noise singular values than signal singular values in traditional FRI algorithms was analyzed in (Wei and Dragotti 2015). Hence, to overcome this problem, we have used the ResNet-50 architecture as an alternative even though many such deep net architectures can be used for FIR construction (Leung *et al.* 2020) and such networks learn from noisy measurements $\left\{\tilde{f}[n]\right\}_{n=1}^{N}$ to FRI parameters $\{t_r\}_{r=1}^{R}$. The advantage of this method is it avoids the occurrence of the larger magnitudes of the noise singular values than signal singular values (i.e. it avoids the subspace swap problem). Moreover, in the traditional subspace methods, sampling kernel information is encoded in $c_{l,n}$ where as the proposed approach does not require such information explicitly. Instead, the network aims to get the information implicitly by training on a large amount of data. The procedure of the proposed approach is as follows.

The continuous-time FRI signal $g(t)$ as a stream of R Diracs. The signal $g(t)$ is filtered with the P^{th} order exponential reproducing kernel in (1.29) which generates the signal $f(t)$. Then the filtered signal $f(t)$ is uniformly sampled which leads to the $f[n]$ in (3.2). By using this sampling procedure, we generate the training data which consists of discrete noisy sample sets as follows.

First, M number of different sample sets $f[n]$ are generated by using M number of different FRI signals $g(t)$. Next, the samples are contaminated with white Gaussian noise of standard deviation σ, this process produces M number of different noisy sample sets $\tilde{f}[n]$ in (3.12). The ground truth parameters are the actual time locations of the M number of different FRI signals $g(t)$ i.e. $\{t_r\}_{r=1}^{R}$. After pre-processing the data, the ResNet-50 model is trained with the training data, that is, model learns the weights from the input noisy measurements $\left\{\tilde{f}[n]\right\}_{n=1}^{N}$ with label parameters $\{t_r\}_{r=1}^{R}$. In this model, we used the Adam optimizer with a learning rate of lr. The loss function used in the proposed reconstruction approach is mean absolute error (MAE), that is,

$$MAE = \frac{1}{R}\sum_{r=1}^{R}|t_r - \hat{t_r}| \tag{3.14}$$

where, t_r is original time locations and $\hat{t_r}$ is predicted time locations. This loss function

minimizes the distance between the original time locations $\{t_r\}_{r=1}^{R}$ and predicted time locations $\{\hat{t_r}\}_{r=1}^{R}$. For testing, the noisy samples $\tilde{f}[n]$ are generated by using the continuous-time FRI signal $g(t)$. After, these noisy samples are given to the proposed reconstruction approach and then retrieve the time locations $\hat{t_r}$ where $r = 1, 2, .., R$.

3.4 Simulation results

3.4.1 Sparse-Prony reconstruction: The noiseless scenario

A stream of $R = 4$ Diracs with time delays t_r =[0.0791, 0.2051, 0.3779, 0.6162] and amplitudes a_r =[3, 2, 2.5, 1.5], respectively, is considered in this experiment. The analog time is quantized with step of $\Delta = \frac{1}{1024}$ second. Fig. 3.2(a) shows an instance of the FRI signal. A plot of the exponential reproducing kernel for $P = 15$ with $\omega_0 = \frac{-P\pi}{N}$ and $\lambda = \frac{2\pi}{N}$ is given in Fig. 3.2(b). The input FRI signal is convolved with the kernel and the output is discretized at a rate $\frac{1}{T} = N$ as depicted in Fig. 3.2(c). The number of measurement samples and duration are taken to be $N = 2(P+1)$ and $\tau = 1$, respectively. The proposed sparse-Prony method is employed to samples to estimate time delays and amplitudes. Reconstructed signal is shown in Fig. 3.2(d), and in the plot, and we observed a perfect reconstruction of the signal upto a numerical precision.

3.4.2 Sparse-Prony reconstruction: The noisy scenario

We simulated several experiments and presented results to evaluate performance of the sparse-Prony method in presence of noise. The method effectiveness is first demonstrated by experimenting with different measurement sample lengths. In this experiment, considered a signal with $R = 3$ Diracs, time delays t_r=[0.2438, 0.2536, 0.2633] and amplitudes a_r =[2, 2, 2], respectively. Measured $N = m(P + 1)$, $m = 2, 3, 4, 5, 6$ uniform samples of the signal, where P is order of the kernel. The i.i.d. Gaussian noise with zero mean and variance σ^2 is used to contaminate the samples. The variance is chosen in accordance with the target SNR defined to be SNR (dB) = 10 $log\frac{\|f\|^2}{N\sigma^2}$. We vary the SNR from 0 dB to 100 dB in steps of 2 dB. Due to the presence of measurement noise, Cadzow denoising method is employed before applying the sparse-Prony method. The time delay estimation performance is compared in terms of average MSE

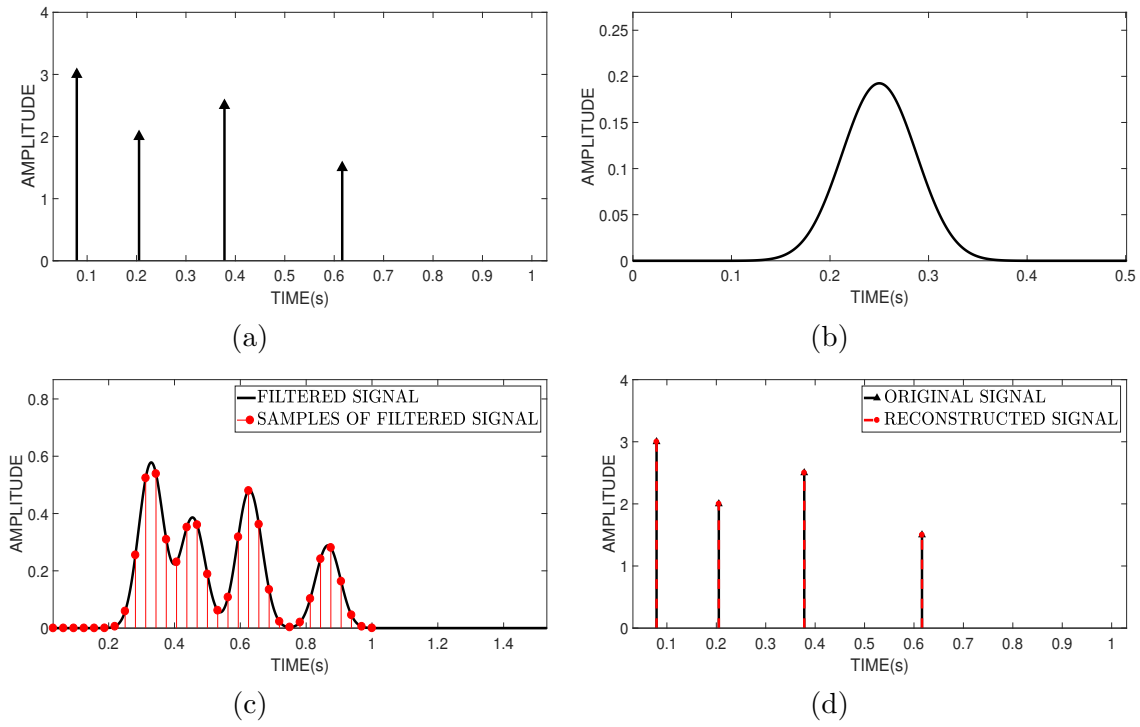

Figure 3.2: (a) Stream of $R = 4$ Diracs, (b) Exponential reproducing kernel with $P = 15$, (c) Filtered signal (black) and its measurement samples (red), and (d) Original (black) and reconstructed (red) signal.

computed over $I = 1000$ instances for each level of noise. The MSE is calculated as

$$MSE = \frac{1}{R}\sum_{r=1}^{R}\left(\frac{1}{I}\sum_{i=1}^{I}\left(t_r - \hat{t}_r^i\right)^2\right) \tag{3.15}$$

where R is the number of Diracs, t_r is true time delay of the Dirac, and $\hat{t}_r^i$ be the estimated time delay of r^{th} Dirac for i^{th} instance of the noise. Fig. 3.3 demonstrates that increasing the SNR results in reduced MSE. The plot also illustrates that when N increases, MSE is also increased. Therefore, $N = 2(P+1)$ is considered for rest of the simulations as it gives more stable $c_{l,n}$ (1.29) coefficients.

Next, we compared performance of the sparse-Prony method to Prony's method and matrix pencil method in various scenarios. The first experiment is based on varying distance between the Diracs δt. For this, two signals are considered with $\delta t = 0.0049$ and $\delta t = 0.0683$. The time delays of the two signals are t_r =[0.2646, 0.2744, 0.2793; 0.2061, 0.2744, 0.3428] and all amplitudes were set to 2. Figs. 3.4(a)-

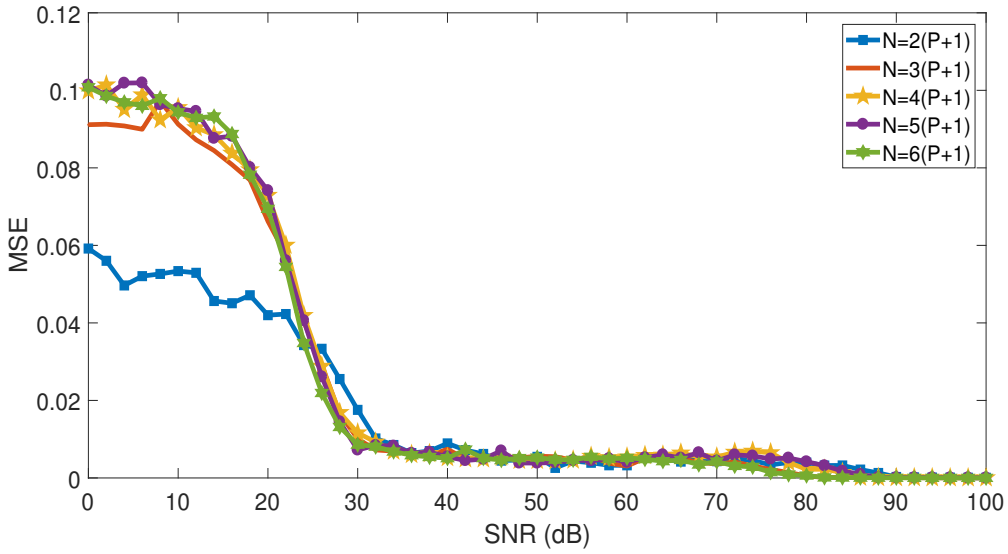

Figure 3.3: Reconstruction in presence of noise for different number of measurement samples N, order of the kernel $P = 15$.

3.4(b) illustrate that when δt is increased, MSE of the sparse-Prony method is decreased. This is because, when the Diracs are closely spaced, the kernel makes them overlap hence not fully-resolving the samples, making reconstruction to become ill-conditioned.

The second experiment is based on varying the order of the kernel P. We considered a signal with $R = 3$ Diracs. The amplitudes are set to 2, and the time delays are t_r =[0.2549, 0.2744, 0.2939]. Figs. 3.5(a)-3.5(b) show that when P increases, MSE of the sparse-Prony method is decreased. The reason is that when order of the kernel P is increased, the number of measurement samples $q[l]$ increases and hence improves the performance in terms of MSE. Moreover, from Figs. 3.4(a)-3.4(b) and Figs. 3.5(a)-3.5(b), we observed a breakdown for SNR below 70 dB in Fig. 3.4(a) and Fig. 3.4(b), 65 dB in Fig. 3.5(a) and 50 dB Fig. 3.5(b). This is due to the fact that these methods are based on computing SVD of the Toeplitz matrix Q. The singular value of the noise becomes greater than that of the signal when noise power increases beyond a certain threshold, and at this stage breakdown occurs. At this breakdown, the sparse-Prony method exhibits better performance than that of the traditional FRI methods. The reason for this is that the sparse-Prony approach avoids solving polynomial roots of the annihilating filter.

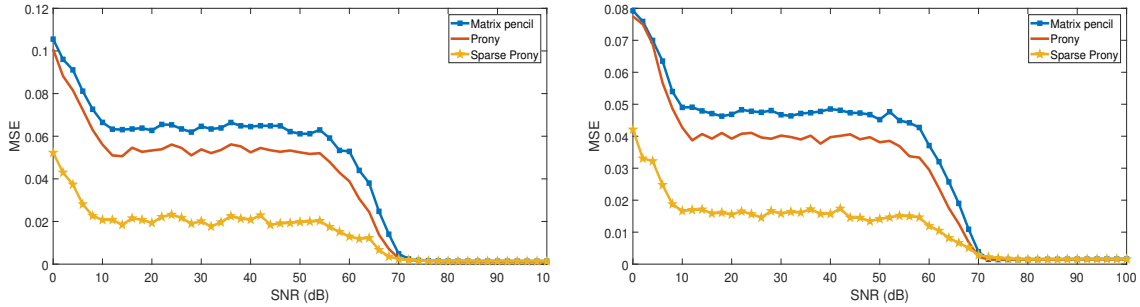

(a) Spacing $\delta t = 0.0049$ (b) Spacing $\delta t = 0.0683$

Figure 3.4: Reconstruction in presence of noise for different spacing δt, order of the kernel $P = 15$.

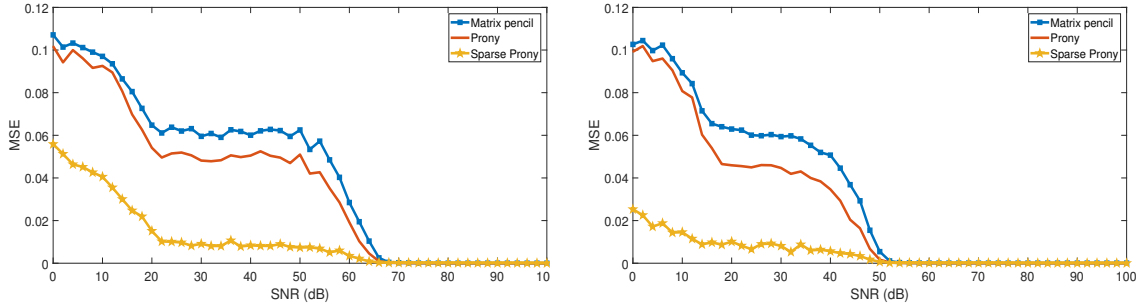

(a) $P = 15$ (b) $P = 21$

Figure 3.5: Reconstruction in presence of noise for different order of the sampling kernel P.

The third experiment is based on varying the levels of sparsity R. Assumed constant amplitudes and time delays to be such that the samples are next to each other. Average MSE of the sparse-Prony and Prony's methods in noisy and noiseless (NL) cases with various sparsity levels are shown in Fig. 3.6. The SNR is set to 15 dB and 20 dB. Fig. 3.6 show that as the level of sparsity R increases, MSE of the sparse-Prony method increases in presence of noise and is zero in the absence of noise. Moreover, Fig. 3.6 demonstrates that increasing the SNR results in reduced MSE. In addition, we also observed that the proposed sparse-Prony method gave a superior reconstruction accuracy than the Prony's method at each level of sparsity, irrespective of the SNR.

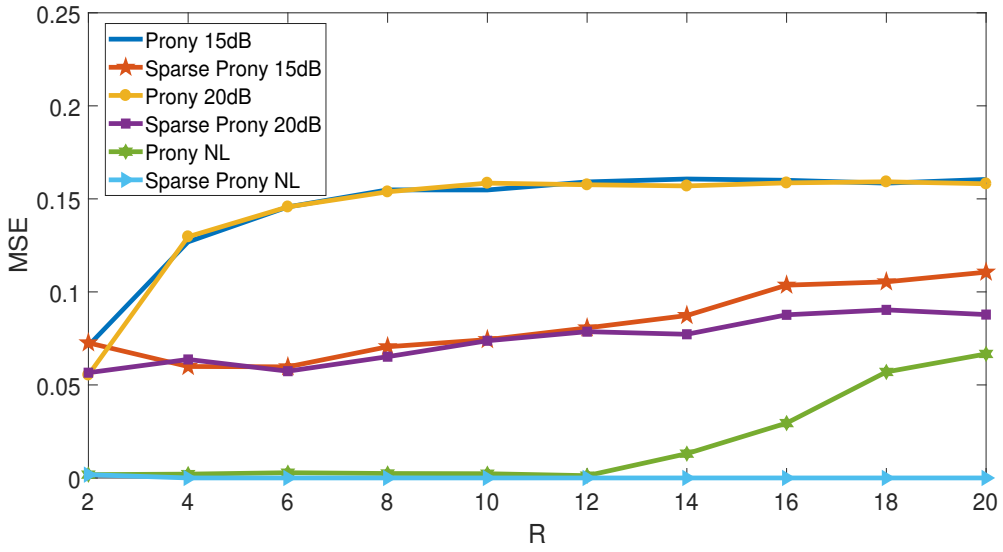

Figure 3.6: Reconstruction in presence and absence of noise for various sparsity levels R, order of the kernel $P = 50$.

3.4.3 ResNet reconstruction: The noisy scenario

To measure and compare performance of our proposed algorithm with the existing FRI algorithms, we simulate the following experiment: Consider the E-spline sampling kernel of order $P = 10$. The number of sample values and length of the signal are fixed to $N = 22$ and $\tau = 1$. Based on the sampling process, the training data set is generated as follows.

First, $M = 10000$ sample sets are generated by using $M = 10000$ FRI signals. Each FRI signal consists of $R = 2$ Diracs. The time locations of Diracs are generated from uniform distribution $[t_1, t_2] \in U[0.3999, 0.7550]$ and corresponding amplitudes are $[a_1, a_2] = [1, 1.5]$. Next, the sample values are corrupted with Gaussian noise which leads to $M = 10000$ noisy sample sets. The procedure was repeated for every SNR $\in [0, 30]$ dB with step size of 1 dB. The ground truth parameters are the actual time locations of the $M = 10000$ different FRI signals $g(t)$. From this data, 96% for each SNR is taken for training the ResNet-50 and 4% for validation. The parameters used in the training are given in the Table 3.1.

For testing, two Diracs are considered with amplitudes $[a_1, a_2] = [1, 1.5]$. We then fix the time location of the first Dirac at $t_1 = 0.4709$ and the time location of the second Dirac is different for two signals, i.e. one at $t_2 = 0.5561$, other is at

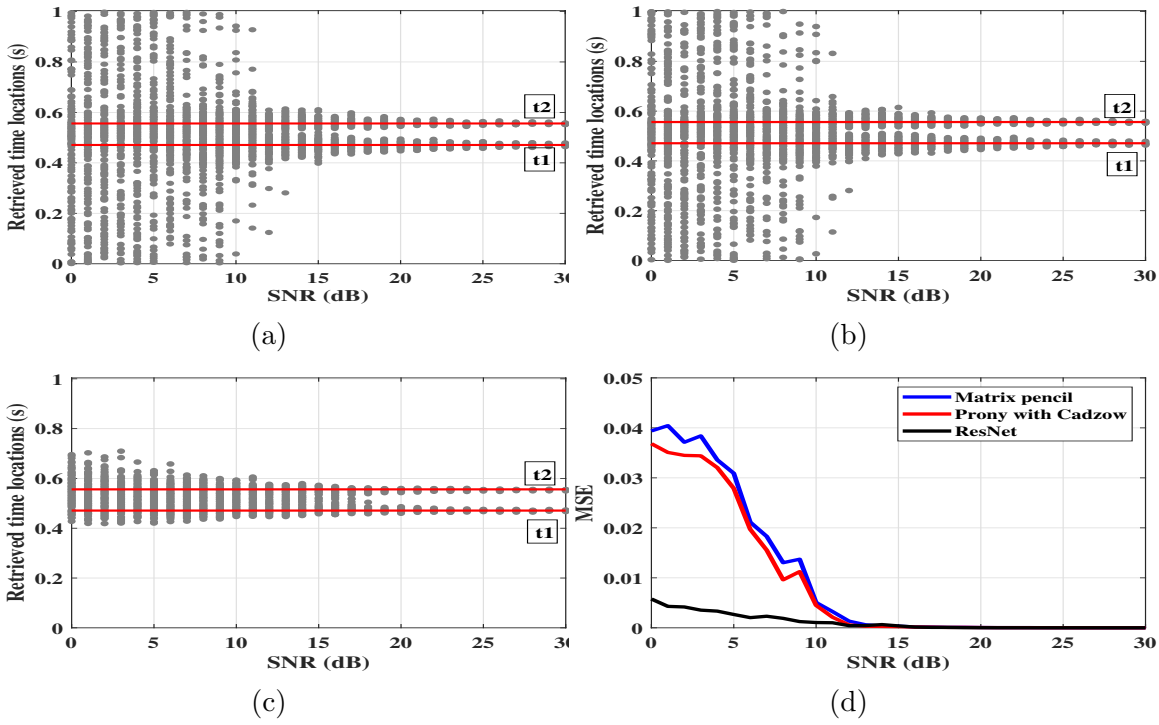

Figure 3.7: Scattered and MSE plots of the retrieved locations over 100 trials at each SNR, where the horizontal lines in (a), (b), (c) represent the actual time values of the Diracs at $t_1 = 0.4709$, $t_2 = 0.5561$.

$t_2 = 0.5774$. These two Diracs are filtered and then uniformly sampled which gives the noisy samples. After, these noisy samples are given to ResNet-50 model and then we retrieve the time locations. In order to compare the ResNet-50 model with existing FRI algorithms, the procedure is repeated 100 times for each SNR value. The simulation results are shown in Fig. 3.7 and Fig. 3.8 where (a) shows the retrieved time locations using matrix pencil method, (b) shows the retrieved time locations using Prony's method with Cadzow algorithm, (c) shows the retrieved time locations using the Resnet-50 and (d) shows the comparison between the average MSE of each method. From Fig. 3.7 and Fig. 3.8, the scattered values at low SNR (breakdown SNR) in (c) are well aligned with the actual time locations compared to the case in (a) and (b). Moreover, from (d) we observe that the ResNet-50 model provides better average MSE than the traditional algorithms in the low SNR range (breakdown SNR). These results indicate that the ResNet-50 architecture has given a higher reconstruction accuracy than traditional FRI algorithms.

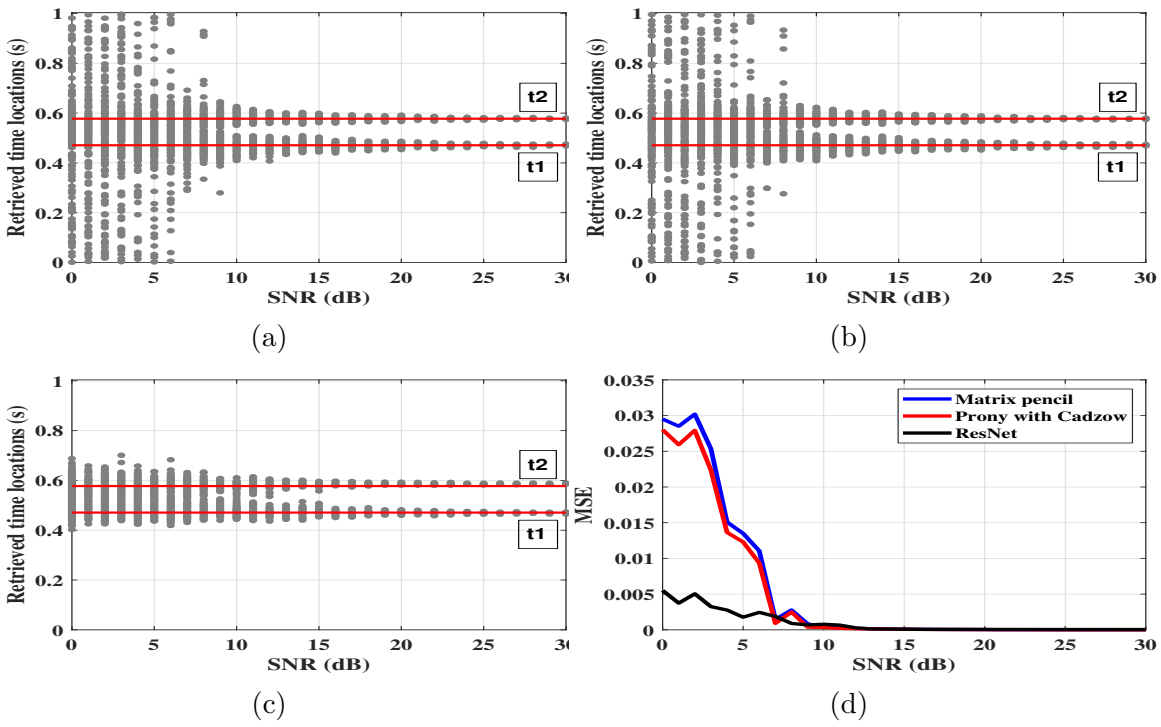

Figure 3.8: Scattered and MSE plots of the retrieved locations over 100 trials at each SNR, where the horizontal lines in (a), (b), (c) represent the actual time values of the Diracs at $t_1 = 0.4709$, $t_2 = 0.5774$.

3.5 Application: Spike detection in two-photon calcium imaging

A major challenge in computational neuroscience is determining the timing of spike trains from neurophysiological data which allows to analyse spatiotemporal activity of neural networks in the brain. Compared to conventional electrophysiological methods, the identification of action potentials (spikes) via two-photon calcium imaging data has certain advantages because it allows for the simultaneous recording of up to thousands of geographically and immunohistochemically identified neurones. FRI framework can be extended for the estimation of spikes in two-photon calcium imaging. Since the two-photon calcium imaging data is modeled as a convolution of the spike train (train of Diracs) with the well-known characteristic pulse i.e decaying exponential representing a signal having an FRI (Onativia *et al.* 2013*b*).

(Onativia *et al.* 2013*b*) have shown that the Prony's method is used to estimate spike train in two-photon calcium imaging data. An annihilating filter is used in

Table 3.1: Parameters used in the training of ResNet-50 architecture.

Parameters	Values
Number of train examples	297600
Number of valid examples	12400
Number of test examples	3100
Number of samples	22
Batch size	64
Number of model Parameters	838770
epochs	15
Learning rate	0.01

Prony's approach, which necessitates the solution of polynomial roots. As a result, when noise infiltrates two-photon calcium imaging data, estimation performance may degrade. To solve this issue, Prony's approach is preprocessed using Cadzow's iterative denoising algorithm (Blu *et al.* 2008). Additionally, the matrix pencil technique estimates spikes without iteration and exhibits performance similar to that of the Cadzow's iterative denoising incorporates Prony's method (Urigüen *et al.* 2013). These algorithms perform best up to a specific SNR and degrade once the SNR drops below that threshold. The same can happen due to subspace swapping, which happens when orthogonal and signal subspaces are interchanged during noisy situations (Wei and Dragotti 2015). To overcome this problem, we employed a proposed sparse-Prony as briefed in Section 3.2.

3.5.1 FRI theory applied to spike detection

A spike in a neuron generates a calcium transient with a characteristic pulse form in the fluorescence signal of the associated neuron. The signal can be represented as the convolution of the spike train $g(t) = \sum_{r=1}^{R} a_r \delta(t - t_r)$ with the well-known characteristic pulse form i.e decaying exponential $p(t) = e^{-\eta t} u(t)$, such that

$$e(t) = g(t) * p(t) = \sum_{r=1}^{R} a_r e^{-\eta(t-t_r)} u(t - t_r), \tag{3.16}$$

where $e(t)$ is an illustration of an FRI signal and is defined by the parameters $\{a_r, t_r\}_{r=1}^{R}$.

As given in the model of Fig. 1.1, signal $e(t)$ is filtered with an exponential

reproducing kernel of $\varphi(t)$ (1.20) and then uniformly sampled at intervals of time $t = nT$. The resulting samples $f[n]$ is expressed as

$$f[n] \;=\; \left\langle e(t), \varphi\left(\frac{t}{T} - n\right)\right\rangle. \tag{3.17}$$

Sampling the signal $e(t)$ with $\varphi(t)$ and determining the subsequent finite differences

$$v[n] = f[n] - e^{-\eta T} f[n-1] \tag{3.18}$$

is identical to sampling the stream of Diracs $g(t)$ with the kernel

$$\Phi(t) = \kappa_{-\eta T}(-t) * \varphi(t) \tag{3.19}$$

where $\kappa_{-\eta T}(-t)$ is E-spline of zero order with parameter $-\eta T$ (Onativia *et al.* 2013*b*). The exponential reproduction property is preserved via convolution, hence $\Phi(t)$ reproduces the same exponentials as $\varphi(t)$. That is, coefficients $d_{l,n}$ exist such that

$$\sum_{n\in\mathbb{Z}} d_{l,n}\Phi(t-n) = e^{j\omega_l t}. \tag{3.20}$$

Note that these $d_{l,n}$ coefficients generally differ from the $c_{l,n}$ coefficients. The estimation of spikes and the reconstruction of a FRI signal, a stream of Diracs $g(t)$ are identical problems. In fact, the sample set $v[n]$ that we have is exactly the same as the sample set obtained by sampling the signal $g(t)$ with the kernel $\Phi(t)$. As a result, the proposed sparse-Prony technique is employed to get the parameters of Diracs $g(t)$ from samples $v[n]$.

3.5.2 Performance of sparse-Prony in absence of noise

In this section we present the performance of the sparse-Prony method with synthetic data. The calcium transient time series is generated $e(t)$ as a stream of $R = 3$ decaying exponentials with parameter $\eta = 10$, time delays t_r =[0.0996, 0.1494, 0.1992] and amplitudes a_r =[2, 2.5, 1.7], respectively (Fig. 3.9(a)). The analog time is quantized with step of $\Delta = \frac{1}{1024}$ second. Sampling is performed using an exponential reproducing kernel $\varphi(t)$ with $P = 15$, $w_0 = \frac{-\pi P}{P+1}$ and $\lambda = \frac{2\pi}{P+1}$, respectively (Fig. 3.9(b)). The filtered output $f(t)$ and its samples $f[n]$ taken at a rate $\frac{1}{T} = N$ second are displayed

in Fig. 3.9(c), where $N = 2(P + 1)$. From these samples, compute weighted finite differences $v[n]$ (Fig. 3.9(c)). The reconstructed and original spikes are depicted in Fig. 3.9(d). The plot illustrates that reconstruction is exact to numerical precision.

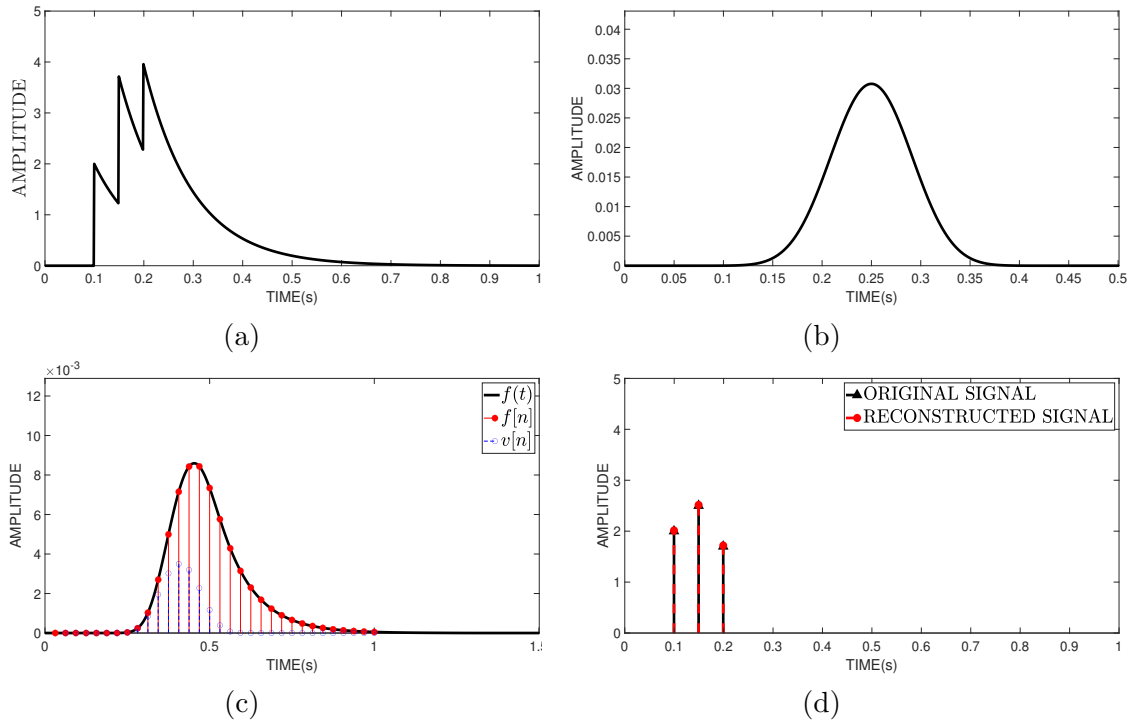

Figure 3.9: (a) Stream of three decaying exponentials, (b) Exponential reproducing kernel with $P = 15$, (c) Filtered signal (black) and its measurement samples (red) and weighted finite differences (blue), and (d) Original (black) and reconstructed (red) spikes.

3.5.3 Performance of sparse-Prony in presence of noise

The previous input is considered as calcium transient time series and measured $N = 2(P + 1)$ samples of the signal, where $P = 15$. The samples are corrupted by i.i.d Gaussian noise with variance σ^2 such that the SNR ranges from 1 dB to 100 dB. Proposed sparse-Prony, Prony's and matrix pencil methods are employed to estimate the time delay parameters of signal. Fig. 3.10 shows the results obtained from averaging 1000 realizations. We observed that all the methods achieve optimal results and perform very similarly for the SNR range of 90 to 100 dB. The performance breaks down when SNR drops outside that range. At this breakdown, the proposed sparse-Prony approach exhibit better performance than Prony's and matrix pencil methods.

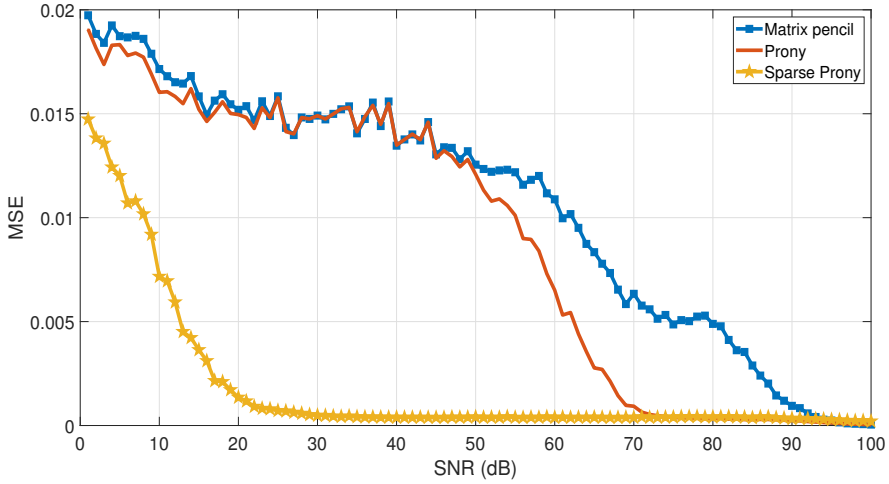

Figure 3.10: Performance comparison in the estimation of t_r. The parameters of the FRI signal are $R = 3$, $t_r = [0.0996 \quad 0.1494 \quad 0.1992]$ and $a_r = [2 \quad 2.5 \quad 1.7]$.

3.6 Summary

In this chapter, we have presented a sparse-Prony approach for reconstructing stream of Diracs based on sparse representation of measurements which avoids solving polynomial roots of the annihilating filter. Further, residual network approach is demonstrated for reconstructing streams of Diracs. Additionally, an application of the sparse-Prony approach on two-photon calcium imaging is demonstrated. The effectiveness of the proposed methods has been verified by simulation results.

Chapter 4

APPROXIMATE FRI-BASED SEISMIC REFLECTIVITY ESTIMATION

4.1 Introduction

In reflection seismology, reflectivity inversion is a crucial deconvolution problem that aids in describing the subsurface structure. The subsurface is built as having sparse reflectivity localized at the boundaries between two layers, taking largely parallel and horizontal layers with piecewise-constant impedance. A 3-layer subsurface model is depicted in Fig. 4.1, which consists of a layer of shale at the top and bottom of a wet sandstone (Russell 2019). The reflection coefficients a_r at the boundary between adjacent layers r and $r+1$ are associated to the subsurface geology (Oldenburg *et al.* 1983) by the relation:

$$a_r = \frac{I_{r+1} - I_r}{I_{r+1} + I_r}, \tag{4.1}$$

where I_r is the impedance of the r^{th} layer. Usually, the reflectivity inversion problem is resolved using basis pursuit and hybrid fista least-squares methods (Zhang and Castagna 2011, Pérez *et al.* 2013, Li *et al.* 2020). Recently, deep learning approaches (Adler *et al.* 2021, Das *et al.* 2019, Wu *et al.* 2020, Wang *et al.* 2022) and sparse Bayesian learning (Yuan and Su 2019*a*, Yuan and Wang 2013) have demonstrated the potential of data-driven methods to problem-solving. These techniques often iteratively work on seismic data to estimate reflectivity. This makes these strategies

computationally expensive and may be sluggish to converge.

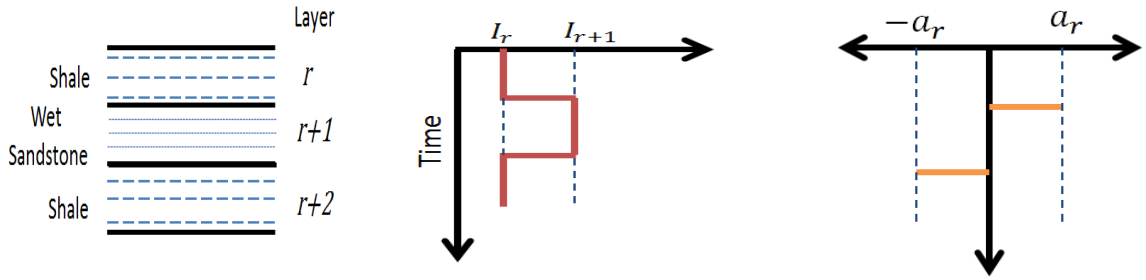

(a) Geology (b) Impedance (c) Reflectivity

Figure 4.1: A 3-layer subsurface model.

In this chapter, a novel method to estimate reflectivity signal in seismic data using an approximate FRI framework is proposed. Assumed the seismic trace as a filtered version of the reflectivity signal with the Ricker wavelet, where the reflectivity is modeled as an FRI signal-a Dirac impulse train with time shifts (locations of boundaries) and amplitudes (reflection coefficients) are considered as the innovations. Unlike deconvolution methods, we demonstrated that estimating reflectivity innovations from a lesser amount of seismic data. The reason for considering approximate FRI in this work is that the Ricker wavelet is the negative second derivative of a Gaussian kernel and this leads to unstable reconstruction when applied to a traditional framework because of their decaying exponent.

The remainder of the chapter is organised as follows. Section 4.2 models the seismic data and describes how estimation of reflectivity signal from seismic data is achieved through approximate FRI framework. Section 4.3 shows simulation results obtained on the synthetic data. Finally, summarize the chapter in Section 4.4.

4.2 Estimation of seismic reflectivity signal using approximate FRI framework

In this section, we introduce modeling of seismic data and method to estimate reflectivity signal from seismic data based on approximate FRI framework.

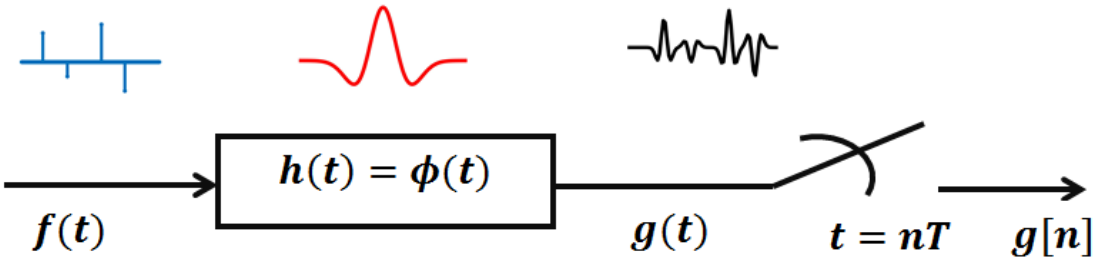

Figure 4.2: Seismic trace model: The input reflectivity signal $f(t)$ is filtered with Ricker wavelet $\phi(t)$ and uniformly sampled with period T. The seismic trace samples are given by $g[n] = f(t) * \phi(t)|_{t=nT}$

4.2.1 Seismic data modeling

Modeling of seismic data is shown in Fig. 4.2. Assuming that the reflectivity $g(t)$ is a finite-length Dirac impulse train

$$f(t) = \sum_{r=1}^{R} a_r \delta(t - t_r), \qquad t_r \in [0, \tau) \tag{4.2}$$

where τ is time duration of reflectivity, R is number of boundaries, $\{t_r, a_r\}_{r=1}^{R}$ correspond to time locations of boundaries and reflection coefficients.

As given in the model, reflectivity $f(t)$ is filtered with Ricker wavelet $\phi(t) = \frac{\alpha^2 - t^2}{\alpha^2} e^{-t^2/2\alpha^2}$ and then sampled every T seconds. The seismic trace samples are given by

$$\begin{aligned} g[n] &= f(t) * \phi(t)|_{t=nT} \\ &= \langle f(t), \phi\left(t - nT\right) \rangle \\ &= \sum_{r=1}^{R} a_r \frac{\alpha^2 - (t_r - nT)^2}{\alpha^2} e^{-(t_r - nT)^2/2\alpha^2}, \end{aligned} \tag{4.3}$$

where $\alpha = 1/2pif_{re}$ is kernel parameter that depends on frequency f_{re}, $n = 1, 2, ..., N$ and $N = \tau/T$. Moreover, assume that $\phi(t)$ is able to reproduce exponentials given by GSFC approximately (Urigüen *et al.* 2013). That is, $\phi(t)$ is a kernel satisfying:

$$\sum_{n \in \mathbb{Z}} d_{p,n} \phi(t - nT) \approx e^{\beta_p t}, \tag{4.4}$$

where $p = 0, 1, ..., L$. The coefficients $d_{p,n}$ in (4.4) are given by

$$d_{p,n} = \frac{1}{\sum\limits_{h\in\mathbb{Z}} e^{-\beta_p hT}\phi(-ht)} e^{\beta_p nT} \tag{4.5}$$

where $\beta_p = j\frac{\pi}{Q}(2p - L)$, $p = 0, 1, ..., L$ and $\frac{\pi}{Q}$ represents the spacing of selected exponential parameters. The error in approximating the exponential is

$$\varepsilon(t) = e^{\beta_p t} - \sum_{n\in\mathbb{Z}} d_{p,n}\phi(t - nT). \tag{4.6}$$

Having obtained a set of seismic data samples $g[n]$ as described above, the task is to estimate reflectivity $f(t)$ from the seismic data samples.

4.2.2 Estimation of reflectivity from seismic data

Signal, reflectivity, is estimated from a set of seismic data measurement samples $g[n]$ as follows:

1 First, new seismic trace samples $q^0[p]$ are obtained by combining samples $g[n]$ (4.3) with coefficients $d_{p,n}$ (4.5) (Dragotti *et al.* 2007), and is expressed as

$$\begin{aligned} q^0[p] &= \sum_{n=1}^{N} d_{p,n} g[n] \\ &= \sum_{n=1}^{N} d_{p,n} \left\langle f(t), \phi\left(t - nT\right)\right\rangle \\ &= \left\langle f(t), \sum_{n=1}^{N} d_{p,n}\phi\left(t - nT\right)\right\rangle \\ &= \left\langle f(t), e^{\beta_p t} - \varepsilon(t)\right\rangle \\ &= \sum_{r=1}^{R} a_r e^{\beta_p t_r} - \sum_{r=1}^{R} a_r \varepsilon(t_r). \end{aligned} \tag{4.7}$$

Due to the approximation error of (4.6), there exists a model mismatch, which is equivalent to $\sum\limits_{r=1}^{R} a_r\varepsilon(t_r)$ and is determined by the kernel $\phi(t)$, coefficients $d_{p,n}$, and parameters β_p and L.

2 Then, set $q^i[p] = q^0[p]$ and iteration number is $i = 1$. If $L \geq 2R-1$, the unknown

reflectivity innovations can be estimated from samples $q^i[p]$ using Prony's, matrix pencil, and sparsity-based method. Note that the approximate framework work with new samples $q^0[p]$, thus, stochastic algorithms are not considered for estimating the reflectivity innovations.

3 Using Prony's method, reflectivity innovations are determined as described; from $\beta_p = j\frac{\pi}{Q}(2p - L)$, $p = 0, 1, ..., L$, we have

$$q^i[p] = \sum_{r=1}^{R} b_r \mu_r^p, \qquad p = 0, 1, ..., L, \tag{4.8}$$

where $b_r = a_r e^{-j\pi L t_r/Q}$ and $\mu_r = e^{j2\pi t_r/Q}$. Consider filter $\mathbf{d}^i$ with R zeros at μ_r in Z-transform $D^i(z) = \prod_{r=1}^{R}(1 - \mu_r z^{-1})$. It clearly follows that

$$q^i[p] \star \mathbf{d}^i[p] = \sum_{u=0}^{R} \mathbf{d}^i[u] q^i[p - u] = 0. \tag{4.9}$$

The filter $\mathbf{d}^i$ is known as an annihilating filter because it annihilates the sequence of samples $q^i[p]$. The above identity is written in matrix notation as follows

$$\begin{bmatrix} q^i[R] & \dots & q^i[1] & q^i[0] \\ q^i[R+1] & \dots & q^i[2] & q^i[1] \\ \vdots & & \vdots & \vdots \\ q^i[L] & \dots & q^i[L-R+1] & q^i[L-R] \end{bmatrix} \begin{bmatrix} \mathbf{d}^i[0] \\ \mathbf{d}^i[1] \\ \vdots \\ \mathbf{d}^i[R] \end{bmatrix} = 0 = Q^i \mathbf{d}^i \tag{4.10}$$

where Q^i is the Toeplitz matrix of size $(L - R + 1) \times (R + 1)$ and $\mathbf{d}^i$ is the annihilating filter of size $(R + 1) \times (1)$ (Vetterli *et al.* 2002). The filter $\mathbf{d}^i$ is estimated from (4.10) as null-space of Q^i with $\mathbf{d}^i[0] = 1$ and then retrieved μ_r by calculating the polynomial roots of D^i. Given μ_r, the boundary time locations $\hat{t}_r^i$ are estimated since $\mu_r = e^{j2\pi t_r/Q}$. Finally, the reflection coefficients $\hat{a}_r^i$ are determined by solving the system of equations in (4.8). In the noise environment, the samples $q^i[p]$ are preprocessed using Cadzow approach, which in-turn improves the estimate of $\mathbf{d}^i$

4 Using matrix pencil method, reflectivity innovations are determined as described; first, build the Toeplitz matrix Q^i of size $(L-R+2) \times (R)$ from samples $q^i[p]$ in

(4.8). Let Q_1^i, Q_2^i be the matrices created from Q^i by eliminating the first and last rows, respectively. Then, the parameters μ_r are retrieved by eigenvalues of $Q_2^{i+}Q_1^i$, where Q_2^{i+} is pseudoinverse of Q_2^i . Finally, from parameters μ_r and samples $q^i[p]$, reflectivity innovations are estimated by employing the procedure used in Prony's method. In the presence of noise, Q^i is obtained by keeping the R left-singular vectors corresponding to the R biggest singular values in singular value decomposition of noisy Toeplitz matrix Q^i.

5 Using sparsity-based method, reflectivity innovations are determined as described; quantize the analog time with a resolution of Λ as $t = m\Lambda$ with $m = 0, 1, ..., M-1$ and $M = \tau/\Lambda$ and unknown boundary locations t_r is approximated as $t_r = m_r\Lambda$. The samples $q^i[p]$ are reduced to

$$q^i[p] = \sum_{r=1}^{R} a_r e^{\beta_p m_r \Lambda}, \qquad p = 0, 1, ..., L, \tag{4.11}$$

where $m_r \in [0, M-1]$ is discrete value of boundary location t_r. Expression (4.11) is rewritten in matrix form as

$$\begin{bmatrix} q^i[0] \\ q^i[1] \\ \vdots \\ q^i[L] \end{bmatrix} = \begin{bmatrix} 1 & e^{\beta_0\Lambda} & \dots & e^{\beta_0(M-1)\Lambda} \\ 1 & e^{\beta_1\Lambda} & \dots & e^{\beta_1(M-1)\Lambda} \\ \vdots & \vdots & & \vdots \\ 1 & e^{\beta_L\Lambda} & \dots & e^{\beta_L(M-1)\Lambda} \end{bmatrix} \begin{bmatrix} f_0 \\ f_1 \\ \vdots \\ f_{M-1} \end{bmatrix} \tag{4.12}$$

where $[f_0, f_1, ..., f_{M-1}]^T$ is a $M \times 1$ vector, formed by R reflection coefficient innovations $\{a_r\}_{r=1}^R$ and $(M-R)$ zeros. This leads to a sparse representation of the seismic data samples. Identity (4.12) is written as

$$\Delta = BF \tag{4.13}$$

where $\Delta = [q^i[0], q^i[1], ..., q^i[L]]^T \in \mathbb{C}^{(L+1)\times 1}$ is seismic data vector, $B \in \mathbb{C}^{(L+1)\times M}$ is fat matrix, $F = [f_0, f_1, ..., f_{M-1}]^T \in \mathbb{R}^{M\times 1}$ is R-sparse reflectivity vector with nonzero components at indices $\{m_r\}_{r=1}^R$, and corresponding amplitudes are $\{a_r\}_{r=1}^R$.

Solving (4.13) is an NP-hard problem. For example, orthogonal matching pursuit (OMP) algorithm (Baraniuk 2007) iteratively determines the R-sparse re-

flectivity vector. Once the vector F is known, boundary locations are directly estimated as $\hat{t}_r^i = m_r\Lambda$, and reflection coefficients are $\hat{a}_r^i = F(m_r)$ where m_r is discrete value of nonzero component of F.

6 Finally, recalculate the samples for the subsequent iteration $i+1$ by deleting the model mismatch from $q^0[p]$ (4.7) as follows

$$q^{i+1}[p] = q^0[p] + \sum_{r=1}^{R} \hat{a}_r^i \varepsilon(\hat{t}_r^i) \tag{4.14}$$

7 Repeat steps 2 to 5 until convergence of the innovations $\{\hat{t}_r^i, \hat{a}_r^i\}_{r=1}^R$.

To estimate the reflectivity, boundary location and reflection coefficient innovations are thus found. From these innovations, we estimate the reflectivity $f(t)$ signal as

$$\hat{f}(t) = \sum_{r=1}^{R} \hat{a}_r^i \delta(t - \hat{t}_r^i) \tag{4.15}$$

4.3 Simulation results

In this section, we simulated a variety of experiments and provided results to assess the performance of the proposed FRI framework. To validate the performance proposed FRI framework on synthetic data, the 1-D seismic data of the paper (Yuan and Su 2019*b*) is used. Fig. 4.3(a) shows that this model contains R=29 non-zero spikes with a variety of amplitudes. Then, using a f_{re}=30 Hz Ricker wavelet (Fig. 4.3(b)) and a Λ= 1 ms resolution step, a synthetic seismic data is generated (Fig. 4.3(c)). Using the seismic data, measured the seismic data samples $g[n]$ for $n = 1, 2, ..., N$, and then either used the noiseless samples or contaminated them with Gaussian noise of standard deviation σ. The standard deviation is chosen in accordance with the SNR defined to be SNR (dB) = 10 $log\frac{\|g\|^2}{N\sigma^2}$. Next, the new seismic data samples $q^i[p]$ for $p = 0, 1, ..., L$ are calculated from (4.7). Finally, the reflectivity innovations $\{\hat{t}_r^i, \hat{a}_r^i\}_{r=1}^R$ are estimated using iterative algorithm involves Prony's, matrix pencil, and sparsity-based methods. Simulation results for single instances of the sampling and estimation and for average mean squared error (MSE) performance across multiple instances, are presented.

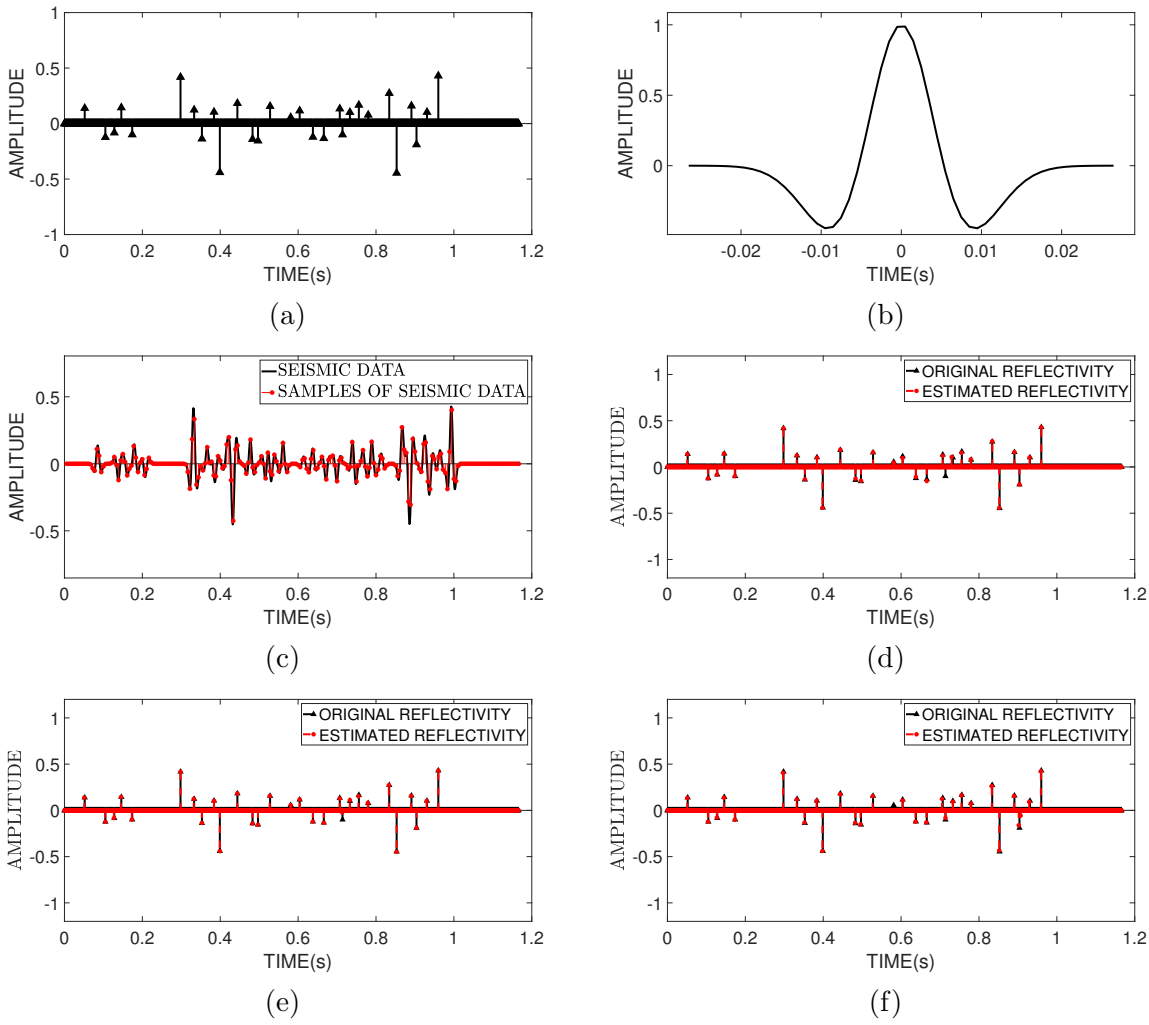

Figure 4.3: Estimation of reflectivity in absence of noise. (a) Original reflectivity. (b) Ricker wavelet sampling kernel. (c) Seismic data and its measurement samples. (d) Original and estimated reflectivity using Prony's method. (e) Original and estimated reflectivity using matrix pencil method. (f) Original and estimated reflectivity using sparsity-based method.

First, the performance of the proposed framework is demonstrated in absence of noise with single instances of the sampling and estimation process. The number of measurement samples and duration are taken to be $N = 210$ and τ=1.167, respectively. To estimate the reflectivity innovations from seismic data, exponential parameters $\beta_p = j\frac{\pi}{Q}(2p - L)$, $p = 0, 1, ..., L$ are used. Prony's, matrix pencil, and sparsity-based methods achieved minimum MSE values approximately at $\frac{Q}{(L+1)T} = 2.1$ with $L = 100$, $\frac{Q}{(L+1)T} = 1.8$ with $L = 100$, $\frac{Q}{(L+1)T} = 1.1$ with $L = 200$, respectively as

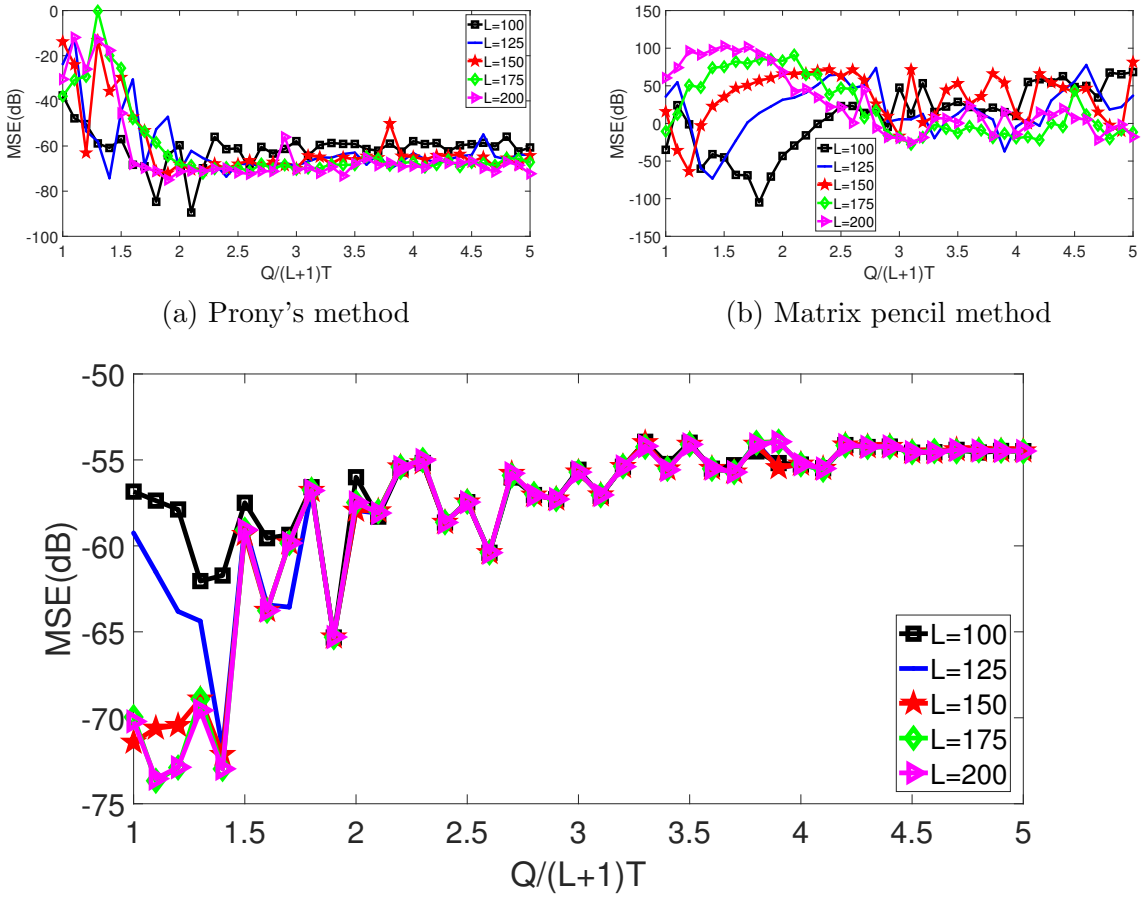

(a) Prony's method

(b) Matrix pencil method

(c) Sparsity-based method

Figure 4.4: Estimation performance of Prony's, matrix pencil, and sparsity-based methods in absence of noise for different possibilities of Q and L.

shown in Fig. 4.4 and the corresponding estimated reflectivity signals are depicted in Fig. 4.3(d), Fig. 4.3(e), and Fig. 4.3(f). Therefore, the above Q values are considered for rest of the experiments as it provides stable $d_{p,n}$ (4.4) coefficients.

Next, the performance of the proposed FRI framework is demonstrated in presence of noise. For this, considered the previous clean seismic data samples and contaminated with signal-to-noise ratio (SNR) of 0 dB to 100 dB in steps of 5 dB. The experiment is repeated 1000 times per each level of SNR, and Fig. 4.5 displays the average estimation MSE result. For SNR greater than 40 dB, matrix pencil method performs better in terms of MSE compared to the Prony's and sparsity-based methods, whereas, for SNR less than 40 dB, the sparsity-based method performs better than matrix pencil and Prony's methods. Moreover, these results suggest that the

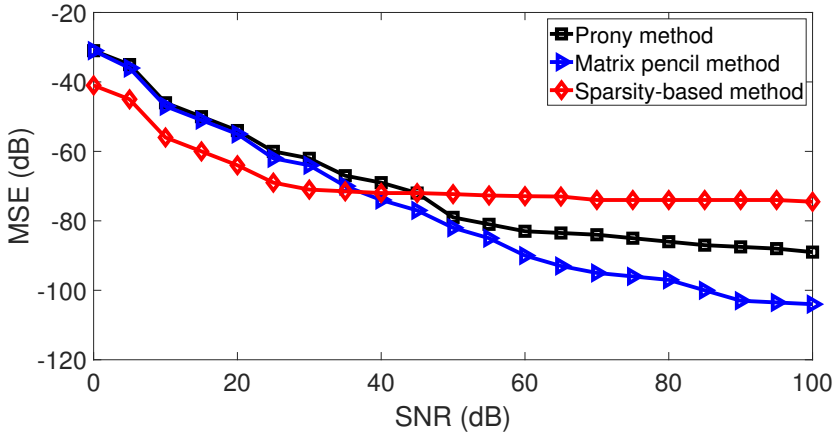

Figure 4.5: Estimation performance of Prony's, matrix pencil, and sparsity-based methods in presence of noise for different levels of noise.

proposed FRI framework has comparable quality of reflectivity estimation, especially in noiseless and medium to high SNR values even though with 5.5 times lesser data than that required by the deconvolution techniques. Note that the deconvolution techniques consider full set of seismic data samples of $g(t)$, i.e $N = 1167$.

4.4 Summary

In this chapter, we presented a novel approach to estimating the seismic data's reflectivity signal using the FRI theory, which aids in understanding the subsurface structure. The convolution of the FRI signal, a Dirac impulse train, and the Ricker wavelet is used to represent the seismic data. The effectiveness of the proposed method has been verified by simulation results.

Chapter 5

CONCLUSION AND FUTURE WORK

5.1 Conclusion

We proposed novel strategies to enhance the performance of FRI algorithms in breakdown caused by subspace swap in discrete-time and continuous-time cases. In particular, in the discrete-time case, using the error decrease detector criterion, a novel universal FRI scheme is proposed for sparse signal reconstruction that works with an unknown number of nonzero coefficients. In absence of noise, exact reconstruction is achievable with minimum number of observations. In the noisy case, simulation results show that the proposed scheme performs better than the traditional scheme especially in breakdown regions and with small numbers of observations. In addition, we have demonstrated an application of the proposed scheme on MR images and QRS complexes which enables MR images and QRS complexes to be reconstructed perfectly in the absence of noise. Moreover, in presence of noise, the proposed scheme has superior reconstruction accuracy than the traditional one at low SNR with less number of observations

Whereas, in the continuous-time case, a novel annihilating filter for reconstructing FRI signals is proposed, based on sparse representation of measurement samples. Simulation results show that the proposed sparse-Prony method achieves perfect reconstruction with undersampled data in the noiseless scenario. In the noisy case, results demonstrate the method to be superior than the traditional methods, especially in breakdown regions, as the method doesn't require finding roots of the annihilat-

ing filter for reconstructing the FRI signal. In addition, we have demonstrated an application of the proposed method to retrieve the timing of action potentials from calcium transient time series which enables detecting spikes perfectly in the absence of noise. Moreover, in presence of noise, the proposed method has high reconstruction accuracy than the conventional methods at breakdown SNR. Further, a novel approach to estimate the FRI signal parameters from the noisy samples using residual neural networks, is presented. The major advantage of the proposed reconstruction approach is that it avoids the occurrence of the larger magnitudes of the noise singular values. Simulation results show the significant improvement in the reconstruction performance compared to that of the traditional FRI methods at breakdown SNR.

Additionally, in the continuous-time case, we have presented an approximate FRI framework for seismic data analysis by modeling reflectivity as an FRI signal. The seismic data is characterized by convolving Dirac impulse trains with the Ricker wavelet. We demonstrated how to develop a suitable kernel using the Ricker wavelet that permits approximate reproduction of exponentials, which is necessary for the approximate FRI framework. Using Prony's, matrix pencil, and sparsity-based methods, we have estimated reflectivity from seismic data samples. The experimental findings show that the suggested FRI method requires almost 5.5 times lesser data than the deconvolution techniques while still producing estimates of comparable quality for noiseless and medium to high SNR regimes.

5.2 Future work

Natural images are sparsely represented in wavelet transform domain, therefore compressive imaging can be performed with fewer measurements by utilising universal FRI. In sonar imaging, image transmission over underwater acoustic channel is challenging because of channel characteristics, such as limited bandwidth. Since sonar images are sparse in bandelet or wavelet transform domain, universal FRI has a fair chance of successfully compressing and transmitting images. Moreover, in radar imaging, the goal is to identify speed, altitude, and direction of steady and moving targets. By solving a reconstruction problem using the universal FRI, received radar signal can be reconstructed from lesser observations. As a result, the price and complexity of receiver's hardware are drastically decreased. Finally, we believe the sparse-Prony algorithm leads to a variety of applications, including compression of ECG and EEG signals,

estimation of spontaneous brain activity in functional MRI, image super-resolution and ultrasound image reconstruction.

Bibliography

Adler, A., **M. Araya-Polo**, and **T. Poggio** (2021). Deep learning for seismic inverse problems: Toward the acceleration of geophysical analysis workflows. *IEEE Signal Processing Magazine*, **38**(2), 89–119.

Baboulaz, L. and **P. L. Dragotti** (2009). Exact feature extraction using finite rate of innovation principles with an application to image super-resolution. *IEEE Transactions on Image Processing*, **18**(2), 281–298.

Baechler, G., **N. Freris**, **R. F. Quick**, and **R. E. Crochiere**, Finite rate of innovation based modeling and compression of ecg signals. *In 2013 IEEE International Conference on Acoustics, Speech and Signal Processing*. IEEE, 2013.

Baraniuk, R. G. (2007). Compressive sensing [lecture notes]. *IEEE signal processing magazine*, **24**(4), 118–121.

Block, K. T. (2008). *Advanced methods for radial data sampling in magnetic resonance imaging*. Ph.D. thesis, Citeseer.

Blu, T., **P. L. Dragotti**, **M. Vetterli**, **P. Marziliano**, and **L. Coulot** (2008). Sparse sampling of signal innovations. *IEEE Signal Processing Magazine*, **25**(2), 31–40.

Brajović, M., **I. Orović**, **M. Daković**, and **S. Stanković** (2017). On the parameterization of hermite transform with application to the compression of qrs complexes. *Signal Processing*, **131**, 113–119.

Cadzow, J. A. (1988). Signal enhancement-a composite property mapping algorithm. *IEEE Transactions on Acoustics, Speech, and Signal Processing*, **36**(1), 49–62.

Cai, J. F., **S. Osher**, and **Z. Shen** (2010). Split bregman methods and frame based image restoration. *Multiscale modeling & simulation*, **8**(2), 337–369.

Chauffert, N., **P. Ciuciu**, and **P. Weiss**, Variable density compressed sensing in mri. theoretical vs heuristic sampling strategies. *In 2013 IEEE 10th International Symposium on Biomedical Imaging*. IEEE, 2013.

Das, V., **A. Pollack**, **U. Wollner**, and **T. Mukerji** (2019). Convolutional neural network for seismic impedance inversioncnn for seismic impedance inversion. *Geophysics*, **84**(6), R869–R880.

Deslauriers-Gauthier, S. and **P. Marziliano**, Magnetic resonance image reconstruction using the annihilating filter method. *In 2011 IEEE International Symposium on Biomedical Imaging: From Nano to Macro*. IEEE, 2011*a*.

Deslauriers-Gauthier, S. and **P. Marziliano**, Magnetic resonance image reconstruction using the annihilating filter method. *In 2011 IEEE International Symposium on Biomedical Imaging: From Nano to Macro*. IEEE, 2011*b*.

Doğan, Z., **T. Blu**, and **D. Van De Ville**, Detecting spontaneous brain activity in functional magnetic resonance imaging using finite rate of innovation. *In 2014 IEEE 11th International Symposium on Biomedical Imaging (ISBI)*. IEEE, 2014.

Donoho, D. L., **A. Maleki**, and **A. Montanari** (2009). Message-passing algorithms for compressed sensing. *Proceedings of the National Academy of Sciences*, **106**(45), 18914–18919.

Donoho, D. L. and **Y. Tsaig** (2008). Fast solution of l_1-norm minimization problems when the solution may be sparse. *IEEE Transactions on Information Theory*, **54**(11), 4789–4812.

Dragotti, P. L., **M. Vetterli**, and **T. Blu** (2007). Sampling moments and reconstructing signals of finite rate of innovation: Shannon meets strang–fix. *IEEE Transactions on signal processing*, **55**(5), 1741–1757.

Elad, M., **P. Milanfar**, and **G. H. Golub** (2004). Shape from moments-an estimation theory perspective. *IEEE Transactions on Signal Processing*, **52**(7), 1814–1829.

Erdozain, A. and **P. M. Crespo** (2010). A new stochastic algorithm inspired on genetic algorithms to estimate signals with finite rate of innovation from noisy samples. *Signal processing*, **90**(1), 134–144.

Erdozain, A. and **P. M. Crespo** (2011). Reconstruction of aperiodic fri signals and estimation of the rate of innovation based on the state space method. *Signal Processing*, **91**(8), 1709–1718.

Feng, L., **R. Grimm**, **K. T. Block**, **H. Chandarana**, **S. Kim**, **J. Xu**, **L. Axel**, **D. K. Sodickson**, and **R. Otazo** (2014). Golden-angle radial sparse parallel mri: combination of compressed sensing, parallel imaging, and golden-angle radial sampling for fast and flexible dynamic volumetric mri. *Magnetic resonance in medicine*, **72**(3), 707–717.

Gilliam, C. and **T. Blu**, Fitting instead of annihilation: Improved recovery of noisy fri signals. *In 2014 IEEE International Conference on Acoustics, Speech and Signal Processing (ICASSP)*. IEEE, 2014.

Gilliam, C. and **T. Blu**, Finding the minimum rate of innovation in the presence of noise. *In 2016 IEEE International Conference on Acoustics, Speech and Signal Processing (ICASSP)*. IEEE, 2016.

He, K., **X. Zhang**, **S. Ren**, and **J. Sun**, Deep residual learning for image recognition. *In Proceedings of the IEEE conference on computer vision and pattern recognition*. 2016.

Hormati, A. and **M. Vetterli**, Annihilating filter-based decoding in the compressed sensing framework. *In Wavelets XII*, volume 6701. International Society for Optics and Photonics, 2007.

Hua, Y. and **T. K. Sarkar** (1990). Matrix pencil method for estimating parameters of exponentially damped/undamped sinusoids in noise. *IEEE Transactions on Acoustics, Speech, and Signal Processing*, **38**(5), 814–824.

Huang, G., **N. Fu**, **J. Zhang**, and **L. Qiao**, Sparsity-based reconstruction method for signals with finite rate of innovation. *In 2016 IEEE International Conference on Acoustics, Speech and Signal Processing (ICASSP)*. IEEE, 2016.

Krizhevsky, A., **I. Sutskever**, and **G. E. Hinton**, Imagenet classification with deep convolutional neural networks. *In Advances in neural information processing systems*. 2012*a*.

Krizhevsky, A., **I. Sutskever**, and **G. E. Hinton**, Imagenet classification with deep convolutional neural networks. *In Advances in neural information processing systems*. 2012*b*.

Kusuma, J. and **V. K. Goyal** (2008). On the accuracy and resolution of powersum-based sampling methods. *IEEE Transactions on Signal Processing*, **57**(1), 182–193.

LeCun, Y., **L. Bottou**, **Y. Bengio**, and **P. Haffner** (1998). Gradient-based learning applied to document recognition. *Proceedings of the IEEE*, **86**(11), 2278–2324.

Leung, V. C., **J.-J. Huang**, and **P. L. Dragotti**, Reconstruction of fri signals using deep neural network approaches. *In ICASSP 2020-2020 IEEE International Conference on Acoustics, Speech and Signal Processing (ICASSP)*. IEEE, 2020.

Leung, V. C., **J.-J. Huang**, **Y. C. Eldar**, and **P. L. Dragotti**, Reconstruction of fri signals using autoencoders with fixed decoders. *In 2021 29th European Signal Processing Conference (EUSIPCO)*. IEEE, 2021.

Li, C., **X. Liu**, **K. Yu**, **X. Wang**, and **F. Zhang** (2020). Debiasing of seismic reflectivity inversion using basis pursuit de-noising algorithm. *Journal of Applied Geophysics*, **177**, 104028.

Lustig, M., **D. L. Donoho**, **J. M. Santos**, and **J. M. Pauly** (2008). Compressed sensing mri. *IEEE signal processing magazine*, **25**(2), 72–82.

Maravic, I. and **M. Vetterli** (2005). Sampling and reconstruction of signals with finite rate of innovation in the presence of noise. *IEEE Transactions on Signal Processing*, **53**(8), 2788–2805.

Markovsky, I. (2008). Structured low-rank approximation and its applications. *Automatica*, **44**(4), 891–909.

Mulleti, S., **S. Nagesh**, **R. Langoju**, **A. Patil**, and **C. S. Seelamantula**, Ultrasound image reconstruction using the finite-rate-of-innovation principle. *In 2014 IEEE International Conference on Image Processing (ICIP)*. IEEE, 2014.

Mulleti, S. and **C. S. Seelamantula**, Periodic non-uniform sampling for fri signals. *In 2015 IEEE International Conference on Acoustics, Speech and Signal Processing (ICASSP)*. IEEE, 2015.

Najjarzadeh, M. and **H. Sadjedi** (2020). Reconstruction of finite rate of innovation signals in a noisy scenario: a robust, accurate estimation algorithm. *Signal, Image and Video Processing*, **14**(8), 1707–1715.

Oldenburg, D., **T. Scheuer**, and **S. Levy** (1983). Recovery of the acoustic impedance from reflection seismograms. *Geophysics*, **48**(10), 1318–1337.

Oñativia, J., **Y. M. Lu**, and **P. L. Dragoni**, Finite dimensional fri. *In 2014 IEEE International Conference on Acoustics, Speech and Signal Processing (ICASSP)*. IEEE, 2014.

Onativia, J., **S. R. Schultz**, and **P. L. Dragotti** (2013*a*). A finite rate of innovation algorithm for fast and accurate spike detection from two-photon calcium imaging. *Journal of neural engineering*, **10**(4), 046017.

Onativia, J., **S. R. Schultz**, and **P. L. Dragotti** (2013*b*). A finite rate of innovation algorithm for fast and accurate spike detection from two-photon calcium imaging. *Journal of neural engineering*, **10**(4), 046017.

Pérez, D. O., **D. R. Velis**, and **M. D. Sacchi** (2013). High-resolution prestack seismic inversion using a hybrid fista least-squares strategy. *Geophysics*, **78**(5), R185–R195.

Poh, K.-K. and **P. Marziliano** (2010). Compressive sampling of eeg signals with finite rate of innovation. *EURASIP journal on advances in signal processing*, **2010**, 1–12.

Russell, B. (2019). Machine learning and geophysical inversion—a numerical study. *The Leading Edge*, **38**(7), 512–519.

Simonyan, K. and **A. Zisserman** (2014). Very deep convolutional networks for large-scale image recognition. *arXiv preprint arXiv:1409.1556*.

Stanković, L., **E. Sejdić**, **S. Stanković**, **M. Daković**, and **I. Orović** (2019). A tutorial on sparse signal reconstruction and its applications in signal processing. *Circuits, Systems, and Signal Processing*, **38**(3), 1206–1263.

Sudhakar Reddy, P., **A. Premkumar**, **B. Saikiran**, **B. S. Raghavendra**, and **A. V. Narasimhadhan**, Finite rate of innovation signal reconstruction using residual neural networks. *In 2020 IEEE 4th Conference on Information & Communication Technology (CICT)*. IEEE, 2020.

Sudhakar Reddy, P., **B. S. Raghavendra**, and **A. V. Narasimhadhan**, Magnetic resonance image reconstruction by nullspace based finite rate of innovation framework. *In Proceedings of the Twelfth Indian Conference on Computer Vision, Graphics and Image Processing*. 2021.

Tan, V. Y. and **V. K. Goyal** (2008). Estimating signals with finite rate of innovation from noisy samples: A stochastic algorithm. *IEEE Transactions on Signal Processing*, **56**(10), 5135–5146.

Tropp, J. A. and **A. C. Gilbert** (2007). Signal recovery from random measurements via orthogonal matching pursuit. *IEEE Transactions on information theory*, **53**(12), 4655–4666.

Urigüen, J. A., **T. Blu**, and **P. L. Dragotti** (2013). Fri sampling with arbitrary kernels. *IEEE Transactions on Signal Processing*, **61**(21), 5310–5323.

Vetterli, M., **P. Marziliano**, and **T. Blu** (2002). Sampling signals with finite rate of innovation. *IEEE transactions on Signal Processing*, **50**(6), 1417–1428.

Wang, Y.-Q., **Q. Wang**, **W.-K. Lu**, **Q. Ge**, and **X.-F. Yan** (2022). Seismic impedance inversion based on cycle-consistent generative adversarial network. *Petroleum Science*, **19**(1), 147–161.

Wei, X. and **P. L. Dragotti**, Universal sampling of signals with finite rate of innovation. *In 2014 IEEE International Conference on Acoustics, Speech and Signal Processing (ICASSP)*. IEEE, 2014.

Wei, X. and **P. L. Dragotti** (2015). Guaranteed performance in the fri setting. *IEEE Signal Processing Letters*, **22**(10), 1661–1665.

Wei, X. and **P. L. Dragotti**, Model order selection for sampling fri signals. *In 2017 IEEE International Conference on Acoustics, Speech and Signal Processing (ICASSP)*. IEEE, 2017.

Wein, A. and **L. Srinivasan** (2013). Iterml: A fast, robust algorithm for estimating signals with finite rate of innovation. *IEEE transactions on signal processing*, **61**(21), 5324–5336.

Wu, B., **D. Meng**, **L. Wang**, **N. Liu**, and **Y. Wang** (2020). Seismic impedance inversion using fully convolutional residual network and transfer learning. *IEEE Geoscience and Remote Sensing Letters*, **17**(12), 2140–2144.

Yuan, C. and **M. Su** (2019*a*). Seismic spectral sparse reflectivity inversion based on sbl-em: experimental analysis and application. *Journal of Geophysics and Engineering*, **16**(6), 1124–1138.

Yuan, C. and **M. Su** (2019*b*). Seismic spectral sparse reflectivity inversion based on sbl-em: experimental analysis and application. *Journal of Geophysics and Engineering*, **16**(6), 1124–1138.

Yuan, S. and **S. Wang** (2013). Spectral sparse bayesian learning reflectivity inversion. *Geophysical Prospecting*, **61**(4), 735–746.

Zhang, R. and **J. Castagna** (2011). Seismic sparse-layer reflectivity inversion using basis pursuit decomposition. *Geophysics*, **76**(6), R147–R158.

Publications based on the thesis

Journal publications:

1. **Sudhakar Reddy, P.**, Raghavendra, B. S., and Narasimhadhan, A. V. (2022). Universal discrete finite rate of innovation scheme for sparse signal reconstruction. *Circuits, Systems, and Signal Processing, Springer*. https://doi.org/10.1007/s00034-022-02220-2
2. **Sudhakar Reddy, P.**, Raghavendra, B. S., and Narasimhadhan, A. V. (2023). Sparse-Prony FRI signal reconstruction. *Signal, Image, and Video Processing, Springer*. https://doi.org/10.1007/s11760-023-02566-3
3. **Sudhakar Reddy, P.**, Raghavendra, B. S., and Narasimhadhan, A. V. (2023). Approximate FRI-based seismic reflectivity estimation. Submitted to *Circuits, Systems, and Signal Processing, Springer*.

Conference publications:

1. **Sudhakar Reddy, P.**, Premkumar, A., Saikiran, B., Raghavendra, B. S., and Narasimhadhan, A. V. Finite rate of innovation signal reconstruction using residual neural networks. *In 2020 4th Conference on Information and Communication Technology (CICT)*. IEEE, 2020. DOI: 10.1109/CICT51604.2020.9312079

2. **Sudhakar Reddy, P.**, Raghavendra, B. S., and Narasimhadhan, A. V. Magnetic resonance image reconstruction by nullspace based finite rate of innovation framework. *In 2021 12th Indian Conference on Computer Vision, Graphics and Image Processing (ICVGIP)*. 2021. https://doi.org/10.1145/3490035.3490294

Bio-data

Pokala Sudhakar Reddy
Rajupalem,
Venkata Setti Palli Post,
Badvel Mandal, Kadapa District,
Andhra Pradesh-516501.
Mobile Number: 9885912710
Mail id: sudhakarpokala406@gmail.com

Education:

1. Ph.D. (Signal Processing), National Institute of Technology Karnataka, Surathkal, 2023.
2. M.Tech. (Signal Processing), Sri Venkateswara University College of Engineering (SVUCE), Tirupati, 2017.
3. B.Tech. (ECE), JNTUA College of Engineering, Ananthapur, 2012.